DOE/ET-53088-218 IFSR #218

DYNAMICS AND FLUCTUATION SPECTRA OF ELECTROSTATIC RESISTIVE INTERCHANGE TURBULENCE

R.D. Sydora, J.N. Leboeuf, Z.G. An*
P.H. Diamond, G.S. Lee, and T.S. Hahm
Institute for Fusion Studies
The University of Texas at Austin
Austin, Texas 78712

* Department of Physics, UCLA

November 1985

Dynamics and Fluctuation Spectra of Electrostatic Resistive Interchange Turbulence

R.D. Sydora,[a] *J.N. Leboeuf, Z.G. An, P.H. Diamond, G.S. Lee, and T.S. Hahm*

Institute for Fusion Studies

The University of Texas at Austin

Austin, Texas 78712-1060

Abstract

The saturation mechanism for density and potential fluctuation spectra which evolve from linearly unstable electrostatic resistive interchange modes, are investigated using particle simulations. Detailed comparisons of the nonlinear evolution, saturation levels and resultant spectra between two and three dimensional sheared magnetic field configurations are made. Significant differences appear. The single rational surface, quasilinear-dominated evolution, fluctuation spectrum is adequately described using a density convection model. For the multiple rational surface case, the potential fluctuations are adequately represented by a balance between the nonlinearly modified source (curvature drive) and linear sink (parallel resistive field line diffusion). An accurate description of the density spectrum requires a mode coupling theory based on the two-point density correlation evolution equation.

[a] Present address: Dept. of Physics, University of California, Los Angeles, California 90024

I. Introduction

The resistive interchange or g-mode is believed to be an important ingredient in the construction of a model of anomalous transport in devices which possess average unfavorable curvature, such as the reversed field pinch[1] (RFP), spheromak,[2] and in some cases, the stellarator.[3] Therefore, it is important to understand the nonlinear evolution and saturation of the instability. Significant departures from expectations based on linear and quasilinear theory may result. In the turbulent, saturated phase, the particle fluxes and spectrum of potential and density fluctuations are observed to exhibit such discrepancies.

The earliest investigation of the resistive g-mode was made by Furth, Killeen and Rosenbluth[4] using slab geometry with a gravitational acceleration to model curvature effects. Subsequently, Hall terms,[5] finite Larmor radius effects,[6] diamagnetic drifts,[7] temperature gradients,[8] ion viscosity[9] and compressibility[7,10] effects were included in the linear stability analysis. The quasilinear evolution of the resistive g-mode has been studied for the tearing[11,12] (magnetic) and interchange (electrostatic) parities.[11,12] It was found that magnetic island induced pressure gradient relaxation[11,13] (for the tearing parity) and electrostatic convection induced gradient flattening[11,13,14] (for the interchange parity) are the saturation mechanisms for the two cases, respectively. These relaxations occur over the width of the island or potential eigenmode, both being localized around the mode rational surfaces ($k_{||} = 0$).

A realistic model for laboratory plasmas is a configuration with many overlapping, interacting g-modes localized about different, neighboring mode rational surfaces. Overlapping magnetic islands result, and as a consequence there is enhanced thermal conduction loss. Hender and Robinson[15] have found evidence for this in magnetohydrodynamic (MHD) simulations of tearing parity interchanges in RFP configurations. In this paper we examine the interchange (electrostatic) parity where electrostatic convection processes dominate. We seek to understand the turbulence and associated transport in the presence of density inhomogeneity, magnetic shear and curvature forces. The emphasis in this work

is on achieving a deeper understanding of the nonlinear physical processes using simple models, which are analytically tractable and can be compared with numerical simulations. The simulation results thus assist the development of the theoretical model.

The main results of this investigation can be summarized as follows.

(i) The nonlinear evolution of localized resistive interchange modes in single and multiple rational surface configurations are compared. Arranging the rational surface distribution so that the eigenmodes are closely spaced and strongly overlapping changes the characteristics of the saturation mechanism for the unstable fluctuations relative to the single mode evolution. For the latter case, localized profile relaxation and subsequent potential and density oscillations result from the $\mathbf{E} \times \mathbf{B}$ convection. In the former case, mode coupling processes are important and modify the saturation amplitudes.

(ii) The single rational surface, quasilinear-dominated evolution, fluctuation spectrum is adequately described using a density convection model. The scaling of the saturation amplitudes for $\hat{n}$ and $\hat{\phi}$ exhibit semi-quantitative agreement with the simulation results.

(iii) For the multiple rational surface case, the root-mean-square (rms) potential fluctuation level, $(e\phi/T_e)_{\rm rms}$, is adequately determined by an asymptotic balance between the nonlinearly modified source (curvature drive) and linear sink (parallel resistive field line diffusion). The density spectrum $(n)_{\rm rms}$ must be treated more accurately and a mode coupling theory, based on the two-point density correlation evolution equation, is constructed. The results are in good qualitative agreement with the numerical simulation spectrum.

The remainder of this paper is organized as follows. In Sec. II the simulation model, initial conditions and parameters are introduced. Section III contains the simulation results and Sec. IV presents the nonlinear g-mode theory, including the two-point theory, and comparisons to the numerical simulations. Section V gives the discussion and concluding

remarks.

II. Simulation Model and Configuration

Many important physical processes contributing to the resistive g-mode in a plasma column can be simulated by the simple model of a slab of plasma confined by a sheared magnetic field. The three-dimensional plasma slab model with density inhomogeneity in the x-direction is used for the particle simulations. The destabilizing effect of magnetic field curvature is represented by an effective gravitational field, as shown in Fig. 1. In this model the equilibrium magnetic field lies in the (y,z) plane and is given by $\mathbf{B} = (0, B_0 x/L_s, B_0)$, where L_s is the shear scale length.

The density is assumed to vary in the x-direction and the profile used initially is

$$n(x) = n_0 \kappa L_x \left[e^{-\kappa x}/(1 - e^{-\kappa L_x}) \right] \tag{1}$$

which gives a constant density scale length, $L_n (\equiv -1/\kappa$, where $\kappa = -n'(x)/n)$ and L_x is the system length in the x-direction. No attempt is made to maintain the mean profile in the simulations. In that respect, they differ from the confinement experiments[1] where the mean profile is maintained. The wavenumber along the magnetic field, $k_{||}$, is given by $k_{||} = (k \cdot \mathbf{B})/|\mathbf{B}| = k_z + k_y(x - x_0)/L_s$ and $k_y = 2\pi m/L_y$, $m = 0, \pm 1, \cdots, \pm L_y/2$, $k_z = 2\pi n/L_z$, $n = 0, \pm 1, \cdots, \pm N$. From the condition, $k_{||} = 0$, the rational surfaces are located at

$$x_{mn} = x_0 \pm (n/m)(L_s L_y/L_z). \tag{2}$$

The rational surface location and packing is varied by adjusting the shear strength, system length and mode numbers (m, n).

In order to incorporate magnetic field curvature, we introduce a gravitational field in a direction opposite to the density gradient. This field is defined as

$$\mathbf{g} = m(v_{||}^2 + v_{\perp}^2/2)/L_c \hat{x} \tag{3}$$

where L_c is the curvature scale length used in modelling the curvature drift of charged particles.

The full Lorentz force is used in the particle simulations to move the ions. The guiding-center drift approximation is used for the electron dynamics transverse to the magnetic field.[16] In order to include a finite electron-ion collision frequency a Monte-Carlo collision operator,[17] which correctly simulates small-angle collisions, is used. This particular operator gives a Spitzer value for the resistivity ($\nu_{ei} \propto T_e^{-3/2}$).

The hybrid approach of a two-dimensional spatial grid in the $x-y$ plane and mode expansion in the z-direction is used to represent the electrostatic potential, $\phi(x,y,z)$, and charge density.[18] This allows the use of an extended system in the axial dimension and reduces the number of Fourier modes which must be retained. The potential is assumed to vanish at the endpoints $x = 0$ and $x = L_x$ and is periodic in the y and z-directions.

Typical simulation parameters used are as follows; $L_x \times L_y \times L_z = 12.8\rho_s \times 51.2\rho_s \times 512\rho_s$, sound Larmor radius $\rho_s = 2.5\delta$, finite-particle size $a_x = 1.5\delta$, $a_y = \delta$, $a_z = 32\delta$, where δ is the unit grid spacing, $T_e/T_i = 1$, $m_i/m_e = 100 - 400$, $L_s/L_n = 14 - 28$, $L_n/L_c = 0.01$, $v_e/\omega_{pe}\delta = 0.5$, $\omega_{ce}/\omega_{pe} = 2 - 5$, $\omega_*/\omega_{ci} = 0.043m$, $n_0 = 15$ particles/cell, $k_y\rho_s = 0.12m$, $m = 0, \pm 1, \cdots, \pm 64$, $k_z = 2\pi n/L_z$, $n = 0, \pm 1, \cdots, \pm 8$, $\omega_{ci}\Delta t = 0.04$ and $\nu_{ei}/\omega_* = 10 - 400$. The rational surfaces are located at $x_{mn}/\rho_s = 6.4 \pm 8(n/m)$ and Fig. 2 shows the position of each surface for given (m,n). The initial density profile is superimposed on the same figure. The surfaces are more densely packed near $x_0/\rho_s = 6.4$, because more modes are retained in the y-direction. The rational surfaces are arranged in this pattern because it ensures that localized profile relaxation plays a less dominant role in the evolution of the unstable modes. Furthermore, local profile steepening, which accompanies relaxation at mode resonances, can occur only in the small region at the edge of the simulation domain.

The parity of the resistive g-modes considered is the interchange parity (even $\hat{\phi}$ with respect to the rational surface) which is the fastest growing in slab geometry. The

linear mode width is determined to be $\Delta/\rho_s \simeq 4m^{-1/3}$ from linear theory. This implies that there are approximately nineteen grid points to describe low mode number eigenmodes ($m \simeq 1-3$) and eight grid points for higher mode numbers ($m \gtrsim 10$). The finite particle size cutoff ($k_y a_y \gtrsim 1$) limits the highest resolvable mode number to be $m \simeq 16$. Since the mode widths are broad compared to the rational surface spacing there is strong overlap at very low fluctuation levels.

III. Simulation Results

A. Linear Theory

Before presenting the simulation results, the basic properties of the electrostatic resistive g-mode are reviewed. The dynamics of the g-mode is most easily understood in the context of an electrostatic density convection model.[19] The equations for the perturbed density, $\hat{n}$, and vorticity, $\nabla \times \hat{v} = (\nabla_\perp^2 \hat{\phi}/B)\hat{z}$ are

$$\frac{\partial \hat{n}}{\partial t} + \hat{\mathbf{v}} \cdot \nabla \hat{n} = -\hat{v}_x \frac{\partial \langle n \rangle}{\partial x} \tag{4}$$

$$\frac{n_0}{\omega_{ci} B}\left[\frac{\partial}{\partial t} + \hat{\mathbf{v}} \cdot \nabla\right] \nabla_\perp^2 \hat{\phi} = -\frac{\nabla_\parallel^2 \hat{\phi}}{|e|\eta} - \frac{g}{\omega_{ci}} \nabla_y \hat{n} \tag{5}$$

where $\omega_{ci} = |e|B/m_i c$, g is the curvature term and η is the resistivity. Linearization of Eqs. (4) and (5) gives the eigenmode equation for the perturbed potential,

$$\left(\frac{\partial^2}{\partial \tilde{x}^2} - k_y^2 \rho_s^2\right)\hat{\phi} - \frac{k_y^2 \rho_s^2}{\omega^2}\frac{g}{n_0}\frac{\partial \langle n \rangle}{\partial \tilde{x}}\hat{\phi} - \frac{\omega_{ci} B}{|e|\eta n_0}\frac{k_\parallel^2}{i\omega}\hat{\phi} = 0 \tag{6}$$

with $k_{||} = k_y x/L_s$ and $\tilde{x} \equiv x/\rho_s$. The eigenfunctions are given as $\hat{\phi}_\ell = e^{-\tilde{x}^2/2\Delta^2} H_\ell(\tilde{x}/\Delta)$, $\ell = 0, 1, \cdots$, where H_ℓ are Hermite functions. In the limit $\gamma > \omega_*$, the growth rate

$$\frac{\gamma}{\omega_{ci}} = (k_y g L_s/L_n)^{2/3}(|e|\eta B/n_0)^{1/3}(1/\omega_{ci}) \tag{7}$$

and linear mode width,

$$\Delta/\rho_s = (k_y)^{-1/3}(L_s)^{2/3}(g/L_n)^{1/6}(|e|\eta B/n_0)^{1/3}(1/\rho_s) \tag{8}$$

are straightforwardly determined.

B. Single Rational Surface ($k_z = 0$)

First, we consider the case where a single mode rational surface is located at $x_0/\rho_s = L_x/2\rho_s = 6.4$. In order to justify the neglect of diamagnetic drift effects ($\gamma > \omega_*$ regime), the parameters of Sec. II were used with $m_i/m_e = 100$, $\omega_{ce}/\omega_{pe} = 2$ and $\nu_{ei}/\omega_* = 40$.

Figure 3 shows the time development of several unstable modes with corresponding wavelengths $k_y\rho_s = 0.125m$, $m = 2, 5$ and 7. The potential fluctuations, given in Fig. 3a, and density fluctuations, Fig. 3b, are spatially averaged over the mode widths in the x-direction. The unstable modes ($m \lesssim 16$) grow initially at the linear growth rate given by $\gamma/\omega_{ci} \simeq 0.14m^{2/3}$, from Eq. (7). A plot of the growth rate versus mode number is shown in Fig. 4. The linear mode widths are approximately $\Delta/\rho_s \simeq 3.3m^{-1/3}$ during the early stages of linear growth. After the initial quasilinear mixing phase, the linear mode widths begin spreading at a rate roughly linear in time. This process will be discussed further in the following section.

After growing between one and two orders of magnitude, the fluctuations saturate. From Fig. 3, the density and potential fluctuations remain in phase with each other during saturation, accompanied by the density gradient oscillations. The saturation time of the density and potential fluctuations corresponds to the relaxation time of the density profile over the width of the linear eigenmode. Figure 5 illustrates the contours of constant ion density determined at time steps $\omega_{ci}t = 12, 20$ and 52. In the early stages, the short wavelength modes ($m > 3$) grow the fastest. After saturation, their fluid excitations are convected by the longest wavelength fluctuations ($m \simeq 1 - 3$). The distance they are convected is of the order the largest linear mode width, $\Delta/\rho_s \simeq 3$.

The mechanism of saturation has been discussed previously and outlined in Ref. 13. A set of quasilinear evolution equations was derived using a density convection model based

on Eq. (4) and are rewritten here as

$$\frac{\partial \langle n \rangle}{\partial t} = \frac{\partial}{\partial x}\left[\gamma|\hat{\xi}_x|^2 \frac{\partial \langle n \rangle}{\partial x}\right] \tag{9}$$

$$\frac{\partial \hat{n}}{\partial t} + \frac{\partial}{\partial x}\left[\gamma|\hat{\xi}_x|^2 \frac{\partial \hat{n}}{\partial x}\right] = \hat{v}_x \frac{\partial \langle n \rangle}{\partial x} \tag{10}$$

where $|\hat{v}_x| \simeq \gamma|\hat{\xi}_x|$; $\hat{\xi}_x$ is the displacement of a density element in the x-direction and γ is the linear growth rate. From these relations, the growth of the fluctuations gives rise to a quasilinear evolution of the average density profile. The perturbed density response vanishes when $k_x^2|\hat{\xi}_x|^2 \simeq 1$ and using $k_x^{-1} \simeq \Delta$, it follows that saturation occurs, when $|\hat{\xi}_x| \simeq \Delta$, i.e., the linear mode width. Since the displacement occurs because of $\mathbf{E} \times \mathbf{B}$ motion, the fluctuation level of the modes at saturation is

$$\frac{e\hat{\phi}_k}{T_e} \simeq \left(\frac{\gamma_k}{\omega_{ci}}\right)\left(\frac{\Delta_k}{\rho_s}\right)\left(\frac{1}{k_y \rho_s}\right) \propto m^{-2/3} \tag{11}$$

$$\frac{\hat{n}_k^2}{\langle n \rangle^2} \simeq \frac{\Delta_k^2}{L_n^2} \propto m^{-2/3}. \tag{12}$$

These 'mixing length' estimates are compared with the measured saturation levels, as shown in Fig. 6. The magnitudes of the fluctuation levels agree within a factor of two with the theoretical estimates. It should be noted that the scalings of $\hat{\phi}$ and $\hat{n}$ with mode number appear to be in good quantitative agreement.

In Fig. 7 the local test particle diffusion coefficient, measured over the eigenmode width, is illustrated. This is obtained by selecting a large collection of interacting test particles and determining their guiding center displacement as a function of time. From Fig. 7 the diffusion coefficient is $D \simeq 0.4\rho_s^2\omega_{ci}$ and is consistent with $D \simeq \sum_k k_y^2|\hat{\phi}_k|^2/B^2\gamma_k = \sum_k \Delta_k^2\gamma_k$. The value decreases slightly when the longest wavelength modes severely distort the equilibrium density profile.

C. *Multiple Rational Surface* ($k_z \neq 0$)

The physical process of convective density mixing over an eigenmode width provides an adequate picture of saturation for the single rational surface case. In the multiple

rational surface configuration this picture must be altered because overlapping, closely packed, eigenmodes can modify the fluctuation dynamics. This can occur in two ways. First, the spatial distribution of rational surfaces, and hence the linear eigenmodes, can allow for strong interaction among the different (m, n) helicities. Second, the closely spaced eigenmodes can modify the profile (source) dynamics differently from the localized, quasilinear relaxation process outlined previously.

The main emphasis in the presentation of the simulation results is the comparison between the fluctuation dynamics in single and multiple rational surface models. For the parameters given in the previous section, the three-dimensional simulation has been carried out for $\omega_{ci}t = 0 - 20$.

Figure 8 shows the time evolution of the electrostatic potential for different mode numbers (m, n). Figure 8a illustrates the growth and saturation of long wavelength modes $(k_y\rho_s \simeq 0.2)$ and Fig. 8b describes the shorter wavelengths $(k_y\rho_s \simeq 1)$. The density fluctuations for various helicities are given in Fig. 9. The linear growth rates as a function of mode number are plotted in Fig. 10. They are in good agreement with theory. A comparison of the potential and density time evolution for the different modes, such as $(2, 0)$, reveals that their evolutions are not strongly coupled. This is in contrast to the single rational surface case where localized density gradient 'sloshing' produces a coupled $\hat{\phi} - \hat{n}$ evolution.

In Fig. 11 a comparison of the time evolution of the ion density profiles for single and multiple rational surface configurations is made. The initial and final profiles, when all wavelengths have saturated, are shown. Figure 11a reveals that there is little localized profile relaxation; however, an overall change occurs. This is to be compared with the single rational surface result, Fig. 11b, where the equilibrium profile has clearly flattened over the eigenmode width centered about the mode rational surface at $x_0/\rho_s = 6.4$.

In order to further demonstrate that quasilinear effects are minimal in three dimensions, the spatial variation of the potential fluctuations is examined. Figure 12 shows

the variation of the potential as a function of x at time steps $\omega_{ci}t = 12$ and $\omega_{ci}t = 18$. In Fig. 12a (three dimensions) the mode width exhibits very little temporal variation in the x-direction. Figure 12b (two dimensions) demonstrates that the quasilinear relaxation process has a significant effect on the mode widths, causing them to spread linearly in time.

One further interesting result is the particle positions in the $y - z$ plane, given in Fig. 13. Time steps $\omega_{ci}t = 0, 12$ and 18 were selected. In the saturation phase, local regions of enhanced particle density are observed. These regions of enhanced density persist during the entire duration of the simulation run. The scale size of the regions corresponds to that of the dominant density fluctuation present at the particular time step.

IV. Nonlinear Theory of the G-mode

In this section the physical picture and analytical model of saturation, for the three-dimensional case, are presented. Localized density profile relaxation is no longer the dominant effect. A parcel of density convected a distance comparable to the eigenmode width exhibits a complex motion due to the presence of the neighboring eigenmodes. This leads to turbulent $\mathbf{E} \times \mathbf{B}$ mixing, mode coupling and coupling to parallel ($k_{\|}^2 |\phi_k|^2/\eta$) and perpendicular (ion viscosity) dissipation.

Since the mode width Δ is a function of growth rate γ, Eqs. (7) and (8), the previously derived fluctuation levels using heuristic mixing lengths estimates such as $\hat{n}_k^2/\langle n \rangle^2 \simeq \Delta_k^2/L_n^2$, lack clear physical meaning at saturation ($\gamma \to 0$). Therefore, a more rigorous derivation of the spatial and temporal scales at saturation is necessary.

To investigate the nonlinear dynamics of resistive interchange modes, a set of renormalized equations for $\hat{n}_k$ and $\nabla_\perp^2 \hat{\phi}_k$, which govern the evolution of the test modes, have been derived from Eqs. (4) and (5) using the standard weak coupling closure approximation[20] and can be written as[21,22]

$$\frac{\partial \hat{n}_k}{\partial t} - \frac{\partial}{\partial x}\left[D \frac{\partial \hat{n}_k}{\partial x}\right] = \frac{-k_y \hat{\phi}_k}{B} \frac{\partial \langle n \rangle}{\partial x} \tag{13}$$

$$\frac{\partial}{\partial t}(\nabla_\perp^2 \hat{\phi})_k - \frac{\partial}{\partial x}\left[D \frac{\partial}{\partial x}(\nabla_\perp^2 \hat{\phi})_k\right] + k_y^2 C_k \hat{\phi}_k = \frac{B\omega_{ci}}{|e| n_0} \frac{k_{\|}^2}{\eta} \hat{\phi}_k - gBik_y \frac{\hat{n}_k}{n_0} \tag{14}$$

where $k = (k_y, k_z)$. The turbulent diffusion coefficient is $D = \sum_{k'} {k'_y}^2 |\hat{\phi}_{k'}|^2 / B^2 \Delta\omega_{k+k'}$ and $C_k = \sum_{k'} \left\langle (\nabla_\perp^2 \hat{\phi})_{k'}^2 \right\rangle / B^2 \Delta\omega_{k+k'}$ is a consequence of symmetrization which ensures energy conservation in the renormalized theory. Here $\Delta\omega_{\mathbf{k}+\mathbf{k}'}$ is used to represent the decorrelation rate between the test mode $\mathbf{k}$ and the background mode $\mathbf{k}'$ in multiple-helicity turbulence. Details of the renormalization procedure are given in the Appendix.

Physically, the random convection of density by the turbulent fluctuations appears as a density diffusivity and the same D accounts for the vorticity diffusion. From Eq. (13) the diffusion coefficient, D, and nonlinear mixing length in the saturated state ($\partial/\partial t \to 0$)

can be obtained. Since the saturation is dynamic, the level can be obtained by balancing the linear driving terms with those which serve as an energy sink. This is more transparent if we write the kinetic energy, $E^k = \frac{1}{2}\int d^3x|\nabla_\perp\hat{\phi}|^2$ and $E^n = \frac{1}{2}\int d^3x|\hat{n}|^2$ time evolution equations[21]

$$\frac{\partial E^K}{\partial t} = -\int d^3x \sum_k \left[\frac{B\omega_{ci}}{|e|n_0}\frac{k_\parallel^2|\hat{\phi}_k|^2}{\eta} - gBik_y\hat{\phi}_{-k}\frac{\hat{n}_k}{n_0}\right] \tag{15}$$

$$\frac{\partial E^n}{\partial t} = -\int d^3x \sum_k \hat{n}_k^* \frac{ik\hat{\phi}_k}{B}\frac{\partial\langle n\rangle}{\partial x} - D\int d^3x\left|\frac{\partial\langle n\rangle}{\partial x}\right|^2. \tag{16}$$

From Eq. (16) it is apparent that the density fluctuations cannot saturate in the absence of localized profile relaxation unless collisional or thermal transport (perpendicular or parallel) is present. This effect has been added to the right-hand side of Eq. (16) and gives the balance (by nonlinear coupling) between density gradient drive due to convective $\mathbf{E}\times\mathbf{B}$ motion and collisional dissipation at small scales. The saturation condition for the turbulent energies is given as $\partial E^K/\partial t = \partial E^n/\partial t = 0$.

First, we consider the saturation condition $\partial E^K/\partial t = 0$. When this criterion is satisfied, the resistive field line diffusion balances the curvature drive,

$$-(g/\omega_{ci})k_y\hat{\phi}_{-k}\hat{n}_k \simeq k_\parallel^2|\hat{\phi}_k|^2/|e|\eta. \tag{17}$$

If we take

$$\hat{n}_k \simeq -(ik_y/B)(\partial\langle n\rangle/\partial x)\hat{\phi}_k/(D/\Delta_k^2) \tag{18}$$

from Eq. (13) and substitute this into Eq. (17), we obtain

$$(g/\omega_{ci})(k_y^2|\hat{\phi}_k|^2/B)(\partial\langle n\rangle/\partial x)(D/\Delta_k^2) \simeq \frac{k_y^2\Delta_k^2|\hat{\phi}_k|^2}{|e|\eta L_s^2}. \tag{19}$$

Solving for D gives

$$D = (|e|\eta/B)(L_s^2 g/\omega_{ci})(\partial\langle n\rangle/\partial x) \tag{20}$$

where we note that D is independent of mode number. At saturation, the asymptotic balance of vorticity diffusion and resistive field line diffusion, in Eq. (14), gives rise to a

nonlinear mixing length

$$\Delta_k = (B\omega_{ci}k_y^2/|e|n_0\eta L_s^2 D)^{-1/6}. \tag{21}$$

Using the value of D which is necessary to balance the curvature and resistive term, we obtain from Eq. (20)

$$\Delta_k = (k_y)^{-1/3}(L_s)^{2/3}(g/L_n)^{1/6}(|e|\eta B/n_0)^{1/3} \tag{22}$$

which is equal to the linear mode width for this case. Using the mixing length theory relation in Eqs. (9) and (10), i.e., $\left\langle \hat{\xi}_x \right\rangle_{\rm rms} = \langle D/\gamma_k \rangle_{\rm rms}$, it is straightforward to verify that $\left\langle \hat{\xi}_x \right\rangle_{\rm rms} = \Delta$. Thus the mixing length theory is vindicated. It is also straightforward to verify that $D = \gamma_k \Delta_k^2$, where γ_k is the linear growth rate, since

$$D = \sum_{k'} \frac{k_y'^2 |\hat{\phi}_{k'}|^2}{B^2 \Delta\omega_{k+k'}} = \sum_k \gamma_k \Delta_k^2. \tag{23}$$

Hence, the potential fluctuation level can be estimated by using the mixing length theory results, $D \simeq \sum_k \gamma_{\mathbf{k}} \Delta_k^2$ and $\Delta\omega_{\mathbf{k}} = \left(D/\Delta_k^2\right) \simeq \gamma_k$, and the root mean square value of the potential fluctuation level is given by

$$\left\langle \left| \frac{e\hat{\phi}_k}{T_e} \right| \right\rangle_{\rm rms} \simeq \left(\frac{\gamma_k}{\omega_{ci}} \frac{\Delta_k}{\rho_s} \frac{1}{k_y \rho_s} \right)_{\rm rms}. \tag{24}$$

This accounts for modes centered on different rational surfaces which can interact with a given test mode, and enters any calculation of D because of the spectrum sum.

In Fig. 14 $\langle |e\phi_m/T_e| \rangle_{\rm rms}$, from the simulation, is shown where the root mean square is taken over k_z and an average over the mode width is performed. Comparing with Eq. (24), we find good agreement for the large wavenumber regime and semi-quantitative agreement for the longest wavelength modes. This is to be expected since the slower growing, longer wavelength modes are more affected by mean profile relaxation than the shorter wavelength modes which grow on a time scale faster than the profile relaxation one.

Next, we consider the saturation condition $\partial E^n/\partial t = 0$, which gives the density fluctuation spectrum, $\hat{n}_k^2$. A simple estimate based on Eq. (18) and Eq. (24) gives

$$\hat{n}_k^2 / \langle n \rangle^2 \simeq \Delta_k^2 / L_n^2 \tag{25}$$

where the value of D in Eq. (20) has been used. Since $\Delta_k \propto k_y^{-1/3}$, the wavenumber dependence for the density spectrum is $\hat{n}_k^2 \propto k_y^{-2/3}$. Hence the density spectrum exhibits a weak dependence on mode number. The density fluctuation spectrum obtained from the simulation does not show this weak wavenumber dependence. It is found that the spectrum asymptotically decays at a rate faster than k_y^{-1}.

The discrepancy in the spectrum arises from the value of D used in Eq. (25). Since D has no wavenumber dependence there is insufficient detailed information in the diffusion coefficient to obtain the correct spectrum. In estimating the electrostatic potential fluctuation spectrum the nonlinearly modified source (curvature drive) balances the linear sink (resistive field line diffusion) giving a reasonably accurate wavenumber dependence. For the density fluctuation spectrum where the nonlinearity dominates, the spectrum must be determined more accurately because mode coupling(including incoherent effects) becomes important. To account for these effects, a spectrum equation, valid at intermediate and short wavelengths, can be derived based on the two-point density evolution equation.

From Eq. (16) the following relation, with $\hat{v}_x = \dfrac{ik_y\hat{\phi}_k}{B}$,

$$-\int d^3x \hat{n}_k^* \hat{v}_x \frac{\partial \langle n \rangle}{\partial x} = D \int d^3x \left| \frac{\partial n}{\partial x} \right|^2 \tag{26}$$

holds at the small scales at saturation. For dynamic saturation, a transfer or coupling term must be added to the right-hand side of Eq. (26). In the steady state this must balance the convective term and at small scales the collisional dissipation maintains the balance. Saturation occurs when the long wavelength density spectrum couples to the small scales through the intermediate wavenumbers.

To quantify this physical picture of saturation, we follow a standard two-point analysis of Eq. (4). The bivariate form of the density convection equation is given by

$$\frac{\partial \langle \hat{n}(1)\hat{n}(2)\rangle}{\partial t} + T_{12} = -\left\langle \frac{\nabla_y \hat{\phi}(1)}{B}\hat{n}(2)\right\rangle \frac{\partial \langle n\rangle}{\partial x} \tag{27}$$

where

$$T_{12} = \left\langle \frac{\nabla_1 \hat{\phi}(1)\times \hat{z}}{B}\cdot \boldsymbol{\nabla}_1 \hat{n}(1)\hat{n}(2)\right\rangle + (1 \leftrightarrow 2).$$

The term, T_{12}, represents the turbulent scattering by the convective nonlinearity. The right-hand side of Eq. (27) is the density gradient source of free energy.[23]

In the two-point analysis, the renormalized triplet is replaced by a relative diffusion operator

$$T_{12} \longrightarrow D_- \frac{\partial^2}{\partial x_-^2}\langle \hat{n}(1)\hat{n}(2)\rangle \tag{28}$$

where D_- is the diffusion coefficient in the relative coordinate $x_- = x_1 - x_2$ and

$$D_- = 2D - D^{(1,2)} - D^{(2,1)} \tag{29}$$

with

$$D = \sum_{k'} k_y'^2 |\phi_{k'}|^2 / B^2 \Delta\omega_{k+k'} \tag{30}$$

and

$$D_- = \sum_{k'} k_y'^2 \frac{\left\langle \hat{\phi}(x_1)\hat{\phi}(x_2)\right\rangle}{B^2\Delta\omega_{k+k'}} e^{ik_{0y}y_- + ik_{0z}z_-}. \tag{31}$$

The diffusion coefficients in Eq. (31) represent correlated diffusion whereas Eq. (30) gives the uncorrelated diffusion coefficient. The renormalized triplet approximates the $\mathbf{E}\times\mathbf{B}$ mixing process and vanishes as the relative separation of the two points goes to zero. The source term on the right-hand side of Eq. (27) does not vanish, and remains finite even at zero separation.

It is the relative diffusion which rearranges the mean density in a spatially dependent manner, and constitutes the turbulent mixing process which gives rise to a scale

dependence of the two-point correlation time. In the steady state the two-point correlation is given as the product of the source term with this correlation time

$$\left\langle \hat{n}^2 \right\rangle \simeq \tau_c \left\langle \frac{\nabla_y \hat{\phi}}{B} \hat{n} \right\rangle \frac{\partial \langle n \rangle}{\partial x} \tag{32}$$

in the limit $k_{0x} x_- < 1$, or at very small relative separation. It has been shown that this correlation time increases logarithmically as the scale of separation approaches zero,[24]

$$\tau_c = \frac{1}{2Dk_{0x}^2} \ell n \left[\frac{1}{k_{0x}^2 x_-^2 + k_{0y}^2 y_-^2 + k_{0z}^2 z_-^2} \right] \tag{33}$$

which is the two-point correlation, or density clump, lifetime. Here k_{0x}, k_{0y} and k_{0z} represent the typical wavenumber of resistive interchange turbulence (most probable fluctuation size in turbulence) in the x, y and z directions, respectively. These wavenumbers can be evaluated by taking the rms value over the calculated wavenumber spectrum of turbulence.[23] It is straightforward to verify that $\tau_c > \tau \simeq \Delta/(\hat{v}_x)_{\rm rms}$, where τ is the approximate linear eigenmode correlation time. Therefore, turbulent $\mathbf{E} \times \mathbf{B}$ mixing destroys all but the small scale correlations on the time scale of the linear eigenmode lifetime (approximately the linear growth rate).

Averaging Eq. (32) over the correlation length in x_- and Fourier transforming in (y_-, z_-) gives

$$\left\langle \hat{n}_{k_y}^2 \right\rangle \simeq \left\langle \frac{\nabla_y \hat{\phi} \hat{n}}{B} \right\rangle \frac{\partial \langle n \rangle}{\partial x} 2\pi \frac{k_{0y}}{k_y^2} \left[1 - J_0 \left(\frac{k_y}{k_{0y}} \right) \right]. \tag{34}$$

An average over k_z is made, and the source term is assumed to have a weak wavenumber dependence at small separation.

In the long wavelength limit ($k_y \rho_s << 1$), Eq. (34) gives $\left\langle \hat{n}_k^2 \right\rangle \simeq$ constant and at the intermediate wavenumbers, $\left\langle \hat{n}_k^2 \right\rangle \propto k_y^{-2}$. At smaller scales ($k_y \rho_s \gtrsim 1$), where collisional dissipation dominates, $\left\langle \hat{n}_k^2 \right\rangle \propto k_y^{-3/2}$. The spectrum predicted from the two-point theory is shown in Fig. 15, along with the simulation results. Also shown is the wavenumber dependence from the mixing length estimate. The accuracy of the above analysis is strongest in the intermediate wavenumber regime. Agreement is not expected

for the long wavelength modes since they are the most affected by mean profile relaxation. At wavelengths, $k_y\rho_s \gtrsim 1$, enhanced shielding effects from finite-size simulation particles, as well as finite gyroradius effects, become important. These enhance the dissipative collisional processes at small scales ($k_y\rho_s > 1$).

V. Summary and Conclusions

A model for the saturation and spectrum of localized electrostatic fluctuations which evolve from linearly unstable resistive interchange modes has been developed. Particle simulations are performed in order to examine the dominant nonlinear processes and test an analytical model. Detailed comparisons are made between the single rational surface ($k_z = 0$) and multiple rational surface configurations. In particular, we have focussed on the transition from a quasilinear-type, single mode, convection-dominated system to a system where spatially overlapping linear eigenmodes are present and turbulent, nonlinear convective processes occur.

The signature for these differences arises in the spatial decorrelation lengths (mixing lengths) and decorrelation times. The behavior of these quantities as well as the spectrum of fluctuations has been analyzed in detail. It has been found that an asymptotic balance between vorticity diffusion and parallel resistive field line diffusion provides an adequate estimate of the nonlinear amplitude-dependent, spatial decorrelation length. Assuming the turbulent fluctuations convect or scatter over this length by $\mathbf{E} \times \mathbf{B}$ motion, the saturation amplitudes are determined and agree reasonably well with the simulation results. To explain the density spectrum at saturation the correlated diffusion of neighboring elements, i.e., mode coupling, must be accounted for to obtain the correct spectral dependence. At short wavelengths this leads to a spatially-dependent decorrelation time and modifies the wavenumber dependence at these small scales.

This section concludes with a comparison between the results presented here and

those from a dimensional analysis[25] of Eqs. (4) and (5). The invariance properties of these equations constrain the scaling of the diffusion coefficient. Dimensional analysis of Eqs. (4) and (5) yields the diffusion coefficient in Eq. (20) to within an arbitrary multiplicative constant. Scaling arguments determine the correlation length in the x-direction. A similar, more quantitative result is obtained through the asymptotic balance between the nonlinearly modified source (curvature drive) and linear sink (resistive field line diffusion). Scaling arguments can be used to determine the radial correlation length because of radial asymmetries introduced by parameters such as magnetic shear, density gradients and curvature. In contrast, the symmetry in the y and z-directions means that the identification of natural scale lengths is non-trivial. Indeed, it is difficult to envision how scaling methods can be used to obtain wavenumber spectra for this problem. Thus, the spectrum is calculated with a theory which includes the $k_y - k_z$ interactions. Since we are not dealing with a simple case of linearly unstable modes at long wavelengths and damped modes at short wavelengths, a Kolmogorov inertial range model (i.e., scaling approach) of the spectrum is not applicable. For example, the sources and sinks (damping) of all modes depend on scale lengths in the x-direction which in turn couple to the y-direction scale lengths. A simple mode coupling theory based on the two-point density correlation evolution equation which incorporates these effects, gives a result in good agreement with the simulation results and appears adequate for determination of the spectrum.

Acknowledgments

This research was supported by the U.S. Department of Energy Contract no. DE-FG05-80-ET-53088.

Appendix: Derivation of the Renormalized Equations

Equations (4) and (5), Fourier transformed in the y and z dimensions, can be written as

$$\partial n_{\mathbf{k}}/\partial t + \left\{ \left[\frac{\partial}{\partial x} \left(\sum_{\mathbf{k}'} \left(-ik'_y/B \right) \phi_{-\mathbf{k}'} n_{\mathbf{k}''} \right) - i \left(k_y/B \right) \sum_{\mathbf{k}'} \frac{\partial \phi_{-k'}}{\partial x} n_{\mathbf{k}''} \right] \right.$$
$$- \left[\frac{\partial}{\partial x} \left(\sum_{\mathbf{k}'} \left(-ik'_y/B \right) n_{-\mathbf{k}'} \phi_{\mathbf{k}''} \right) \right.$$
$$\left. \left. - i \left(k_y/B \right) \sum_{\mathbf{k}'} \frac{\partial n_{-\mathbf{k}'}}{\partial x} \phi_{\mathbf{k}''} \right] \right\} = -i \left(k_y/B \right) \phi_{\mathbf{k}} \frac{\partial \langle n \rangle}{\partial x} \qquad (A1)$$

$$\frac{\partial}{\partial t} \left(\nabla_\perp^2 \phi_{\mathbf{k}} \right) + \left\{ \left[\frac{\partial}{\partial x} \left(\sum_{\mathbf{k}} \left(-ik'_y/B \right) \phi_{-\mathbf{k}'} \nabla_\perp^2 \phi_{\mathbf{k}''} \right) - i \left(k_y/B \right) \sum_{\mathbf{k}'} \frac{\partial \phi_{-\mathbf{k}'}}{\partial x} \nabla_\perp^2 \phi_{k''} \right] \right.$$
$$- \left[\frac{\partial}{\partial x} \left(\sum_{\mathbf{k}'} \left(-ik'_y/B \right) \left(\nabla_\perp^2 \phi_{-\mathbf{k}'} \right) \phi_{\mathbf{k}''} \right) \right.$$
$$\left. \left. - i \left(k_y/B \right) \sum_{k'} \left(\frac{\partial}{\partial x} \nabla_\perp^2 \phi_{-\mathbf{k}'} \right) \phi_{\mathbf{k}''} \right] \right\} = k_\parallel^2 \frac{\omega_{ci} B}{|e| \eta n_0} \phi_{\mathbf{k}} - ik_y \frac{gB}{n_0} n_{\mathbf{k}} \qquad (A2)$$

where $\mathbf{k}'' = \mathbf{k} + \mathbf{k}'$, $\mathbf{k} = (k_y, k_z)$, $\nabla_\perp^2 = \dfrac{\partial^2}{\partial x^2} - k_y^2$ and $k_\parallel = k'_\parallel x = k_y x / L_s$.

Equation (A1) and (A2) are renormalized by the standard procedure[20] of substituting the nonlinearly driven fields $n^{(2)}_{\mathbf{k}''}$ and $\phi^{(2)}_{\mathbf{k}''}$ for $n_{\mathbf{k}''}$ and $\phi_{\mathbf{k}''}$. The nonlinearly driven fields satisfy the equations

$$\Delta\omega_{\mathbf{k}''} n^{(2)}_{\mathbf{k}''} + i \left(k''_y/B \right) \frac{\partial \langle n \rangle}{\partial x} \phi^{(2)}_{\mathbf{k}''} = S_1 \qquad (A3)$$

$$\Delta\omega_{\mathbf{k}''} \nabla_\perp^2 \phi^{(2)}_{\mathbf{k}''} - k''^2_\parallel \left(\frac{\omega_{ci} B}{|e| n_0 \eta} \right) \phi^{(2)}_{\mathbf{k}''} + i \left(gB/n_0 \right) k''_y n^{(2)}_{\mathbf{k}''} = S_2 \qquad (A4)$$

Here, S_1 and S_2 (the sources of the driven modes $\mathbf{k}''$) are the direct beat interaction of the test mode $\mathbf{k}$ with background mode $\mathbf{k}'$, and $\Delta\omega_{\mathbf{k}''}$ is the coherence time of $\mathbf{k}$ and $\mathbf{k}'$.

Approximate solutions for the driven modes are

$$n^{(2)}_{\mathbf{k}''} \cong -\frac{1}{\Delta\omega_{\mathbf{k}''}} \left[\left(ik'_y/B \right) \phi_{\mathbf{k}'} \frac{\partial n_{\mathbf{k}}}{\partial x} - \frac{\partial \phi_{\mathbf{k}'}}{\partial x} \left(ik_y/B \right) n_{\mathbf{k}} \right.$$
$$\left. + \left(ik_y/B \right) \phi_{\mathbf{k}} \frac{\partial n_{\mathbf{k}'}}{\partial x} - i \left(k'_y/B \right) \frac{\partial \phi_{\mathbf{k}}}{\partial x} n_{k'} \right] \qquad (A5)$$

$$\nabla_\perp^2 \phi_{\mathbf{k}''}^{(2)} \cong \frac{1}{\Delta\omega_{\mathbf{k}''}} \Bigg[\left(ik'_y/B\right) \phi_{\mathbf{k}'} \frac{\partial}{\partial x} \left(\nabla_\perp^2 \phi_{\mathbf{k}}\right) - i \left(k_y/B\right) \frac{\partial \phi_{\mathbf{k}'}}{\partial x} \left(\nabla_\perp^2 \phi_{\mathbf{k}}\right)$$

$$+ \left(ik_y/B\right) \phi_{\mathbf{k}} \frac{\partial}{\partial x} \left(\nabla_\perp^2 \phi_{\mathbf{k}'}\right) - i \left(k'_y/B\right) \frac{\partial \phi_{\mathbf{k}}}{\partial x} \left(\nabla_\perp^2 \phi_{\mathbf{k}'}\right) \Bigg]. \qquad (A6)$$

As the mode widths of $\mathbf{k}$ and $\mathbf{k}'$ are roughly comparable for the resistive interchange modes under consideration, the terms with $k''_\parallel$ in Eqs. (A3) and (A4) have been neglected. Similarly, the coupling terms with $\mathbf{k}''_y$ have been neglected on the grounds that nonlinear diffusion is primarily a cascading process independent of the driving.

The symmetry of the nonlinear reduced MHD equations allows one to impose $n_{-\mathbf{k}} = n_{\mathbf{k}}$ and $\phi_{-\mathbf{k}} = -\phi_{\mathbf{k}}$, which in turn allows for considerable simplifications.[20] Substituting the driven modes into the nonlinear interaction terms, we finally obtain the renormalized reduced resistive MHD equations which govern the evolution of the test $\mathbf{k}$ modes, i.e., Eqs. (13) and (14) in text.

References

1. H.A. Bodin and A.A. Newton, Nucl. Fusion **20**, 1255 (1980).
2. M.N. Rosenbluth and M.N. Bussac, Nucl. Fusion **19**, 489 (1979).
3. K.C. Shaing and B.A. Carreras, Phys. Fluids **28**, 2027 (1985).
4. H.P. Furth, J. Killeen and M.N. Rosenbluth, Phys. Fluids **6**, 459 (1963).
5. B. Coppi, Phys. Fluids **7**, 1501 (1964).
6. T.E. Stringer, Nucl. Fusion **15**, 125 (1975).
7. J.M. Finn, W.M. Manheimer and T.M. Antonsen, Jr., Phys. Fluids **26**, 962 (1983); T.S. Hahm and Liu Chen, Phys. Fluids **28**, 2432 (1985).
8. C.L. Chang, N.T. Gladd and C.S. Liu, Reversed Field Pinch Theory Workshop, Conference Proceedings, Los Alamos, 1980 (Los Alamos National Laboratory, Los Alamos, NM, 1980), p. 22.
9. T.E. Stringer, Phys. Fluids **10**, 418 (1967).
10. B. Coppi, J.M. Greene and J.L. Johnson, Nucl. Fusion **6**, 101 (1966).
11. D. Schnack, J. Killeen and R.A. Gerwin, Nucl. Fusion **21**, 1447 (1981).
12. T.C. Hender and D.C. Robinson, Nucl. Fusion **21**, 755 (1981).
13. R.D. Sydora, J.N. Leboeuf, Z.G. An, P.H. Diamond and T. Tajima, Phys. Fluids **28**, 425 (1985).
14. B.A. Carreras, P.H. Diamond, M. Murakami, J.L. Dunlap, J.D. Bell, H.R. Hicks, J.A. Holmes, E.A. Lazarus, V.K. Pare, P. Similon, C.E. Thomas, and R.M. Wieland, Phys. Rev. Lett. **50**, 503 (1983).
15. T.C. Hender and D. Robinson, in Plasma Physics and Controlled Nuclear Fusion Research (International Atomic Energy Agency, Vienna, 1982), Vol. 3, p. 417.
16. W.W. Lee and and H. Okuda, J. Comp. Phys. **26**, 139 (1978).
17. R. Shanny, J.M. Dawson and J.M. Greene, Phys. Fluids **10**, 1281 (1967).
18. C.Z. Cheng and H. Okuda, J. Comp. Phys. **25**, 133 (1977).
19. H.R. Strauss, Phys. Fluids **20**, 1354 (1977).

20. P.H. Diamond, R.D. Hazeltine, Z.G. An, B.A. Carreras, and H.R. Hicks, Phys. Fluids **27**, 1449 (1984).

21. Z.G. An, P.H. Diamond and T. Chiueh, Sixth U.S. Symposium on Compact Toroid Research, Conference Proceedings, Princeton, 1984 (Princeton Plasma Physics Laboratory, Princeton, NJ, 1984) p. 259.

22. Z.G. An, P.H. Diamond, R.H. Hazeltine, J.N. Leboeuf, M.N. Rosenbluth, R.D. Sydora, T. Tajima, B.A. Carreras, L. Garcia, T.C. Hender, H.R. Hicks, J. Holmes, V.E. Lynch, and H.R. Strauss, in Plasma Physics and Controlled Nuclear Fusion Research (International Atomic Energy Agency, Vienna, 1984), vol. 2, p. 231.

23. P.W. Terry and P.H. Diamond, Phys. Fluids **28**, 1419 (1985).

24. T.H. Dupree, Phys. Fluids **15**, 334 (1972).

25. J.W. Connor and J.B. Taylor, in Plasma Physics and Controlled Nuclear Fusion Research (International Atomic Energy Agency, Vienna, 1984), vol. 2, p. 13.

Figure Captions

Fig. 1 Schematics of the particle simulation configuration.

Fig. 2 Rational surface positions as a function of x/ρ_s for each mode number (m,n) with initial density profile superimposed.

Fig. 3 Time development of potential and density fluctuations for single rational surface case.

a. Evolution of electrostatic potential, averaged over mode width, for $m = 2, 5$ and 7.

b. Evolution of density, averaged over mode width, for $m = 2, 5$ and 7.

Fig. 4 Linear growth rates versus mode number for single rational surface case.

Fig. 5 Contours of constant ion density in the single mode rational surface case taken at time steps (a) $\omega_{ci}t = 0$, (b) $\omega_{ci}t = 20$ and (c) $\omega_{ci}t = 52$.

Fig. 6 Saturation levels, in the single mode rational surface, as a function of mode number. (a) potential fluctuations and (b) density fluctuations. Solid lines represent theoretical estimates and solid dots the simulation values.

Fig. 7 Local test particle diffusion coefficient measured over the eigenmode width in the single rational surface case.

Fig. 8 Time evolution of the potential fluctuations in the multiple rational surface case, averaged over the mode widths, for modes (a) $(2,n)$ and (b) $(8,n)$.

Fig. 9 Time evolution of the density fluctuations, averaged over the mode width, for modes (a) $(2,0), (5,0)$ and $(9,0)$ and (b) $(3,4), (8,4)$.

Fig. 10 Linear growth rates versus mode number for the multiple rational surface case.

Fig. 11 Comparison between ion density profile evolution in (a) multiple rational surface and (b) single rational surface configurations.

Fig. 12 Comparisons of spatial electrostatic potential evolution for (a) multiple rational surface and (b) single rational surface eigenmodes.

Fig. 13 Ion particle positions in the $y - z$ plane, for the multiple rational surface case, taken at time steps (a) $\omega_{ci}t = 0$, (b) $\omega_{ci}t = 18$ and (c) $\omega_{ci}t = 20$.

Fig. 14 Saturation levels for spatial and n-averaged electrostatic potential fluctuations versus mode number in the multiple rational surface case.

Fig. 15 Saturation levels for spatial and n-averaged density fluctuations versus mode number in the multiple rational surface case.

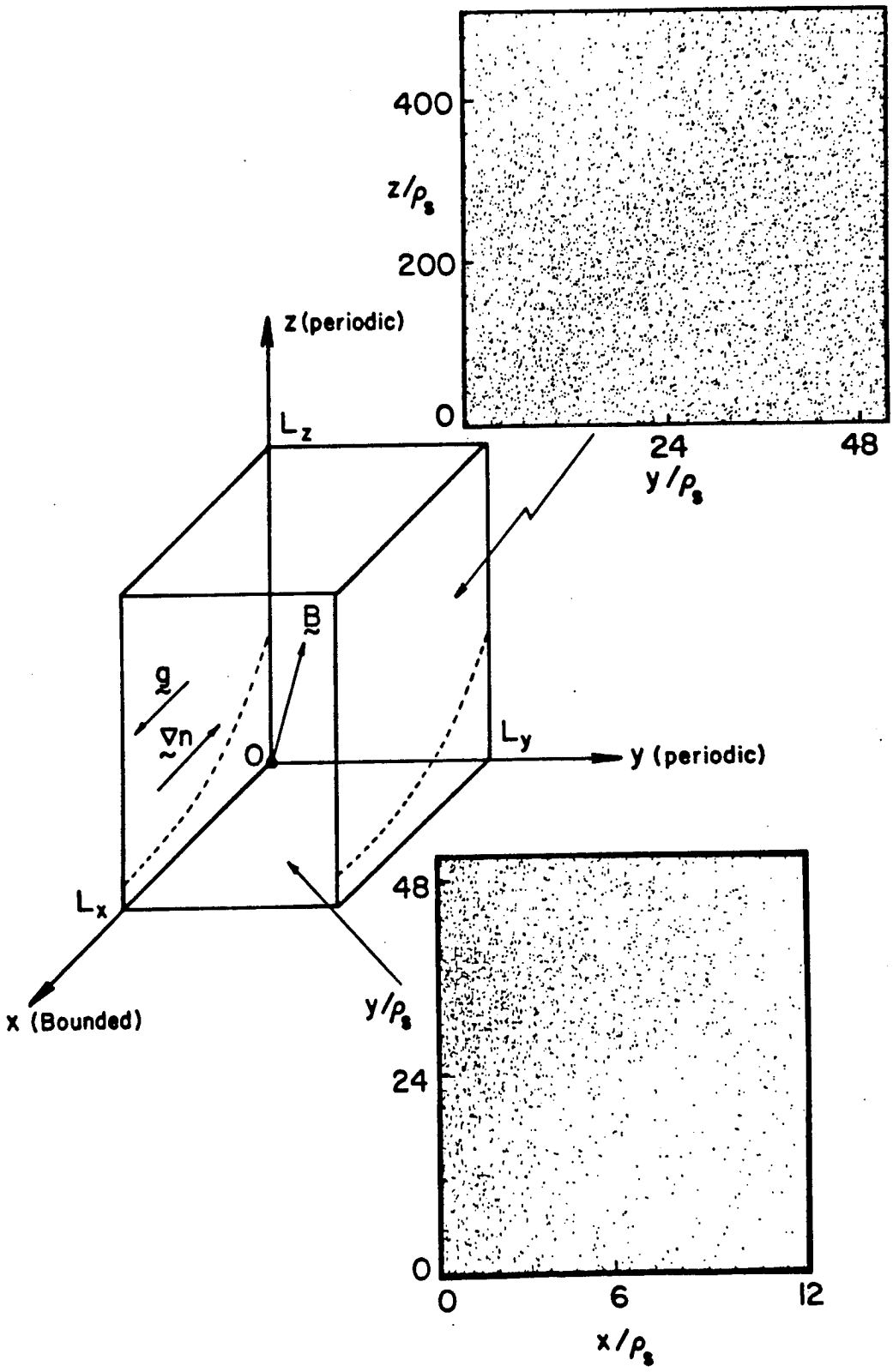
400
z/ρ_s
200
0
24
48
y/ρ_s
z (periodic)
L_z
$\underset{\sim}{B}$
$\underset{\sim}{g}$
$\underset{\sim}{\nabla n}$
O
L_y
y (periodic)
L_x
x (Bounded)
y/ρ_s
48
24
0
0
6
12
x/ρ_s

Fig. 1

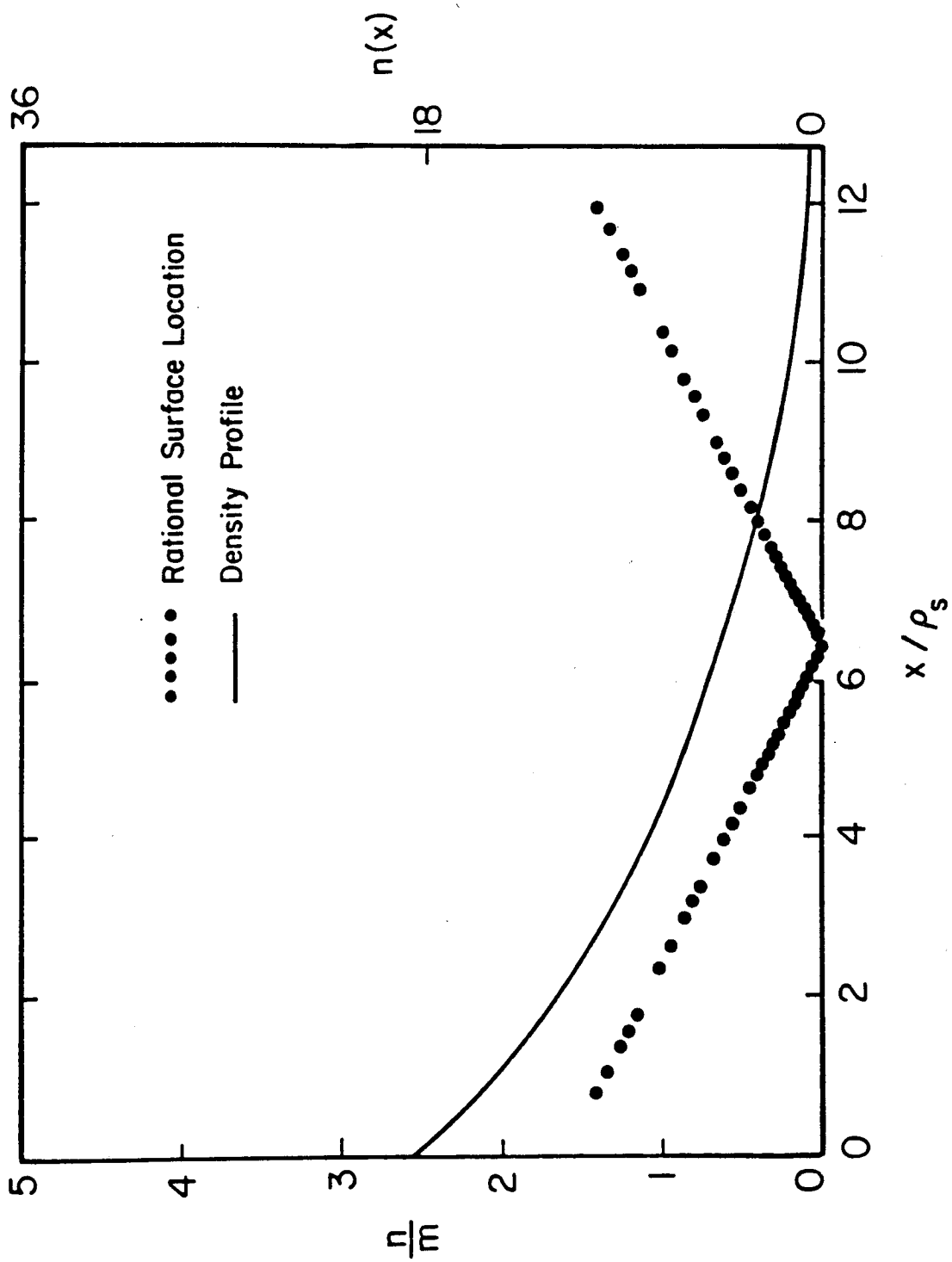
n(x)
36
18
0
Rational Surface Location
Density Profile
5
4
3
2
1
0
n/m
0
2
4
6
8
10
12
x / ρs

Fig. 2

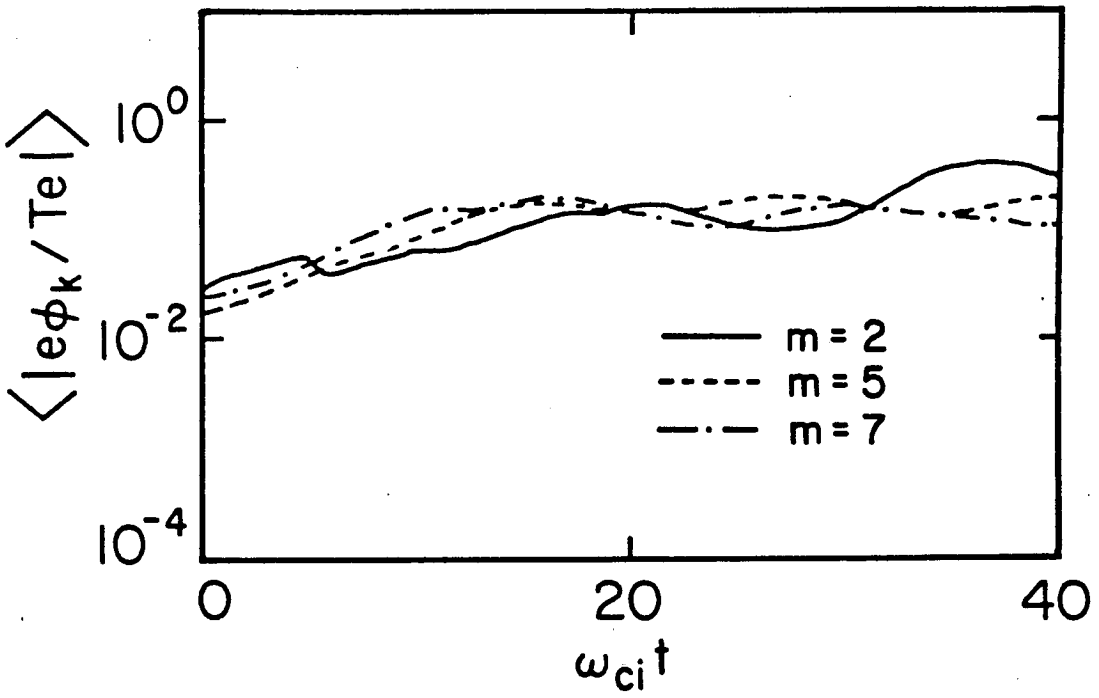
$\langle |e\phi_k / Te| \rangle$
10^0
10^{-2}
10^{-4}
0
20
40
$\omega_{ci} t$
m = 2
m = 5
m = 7

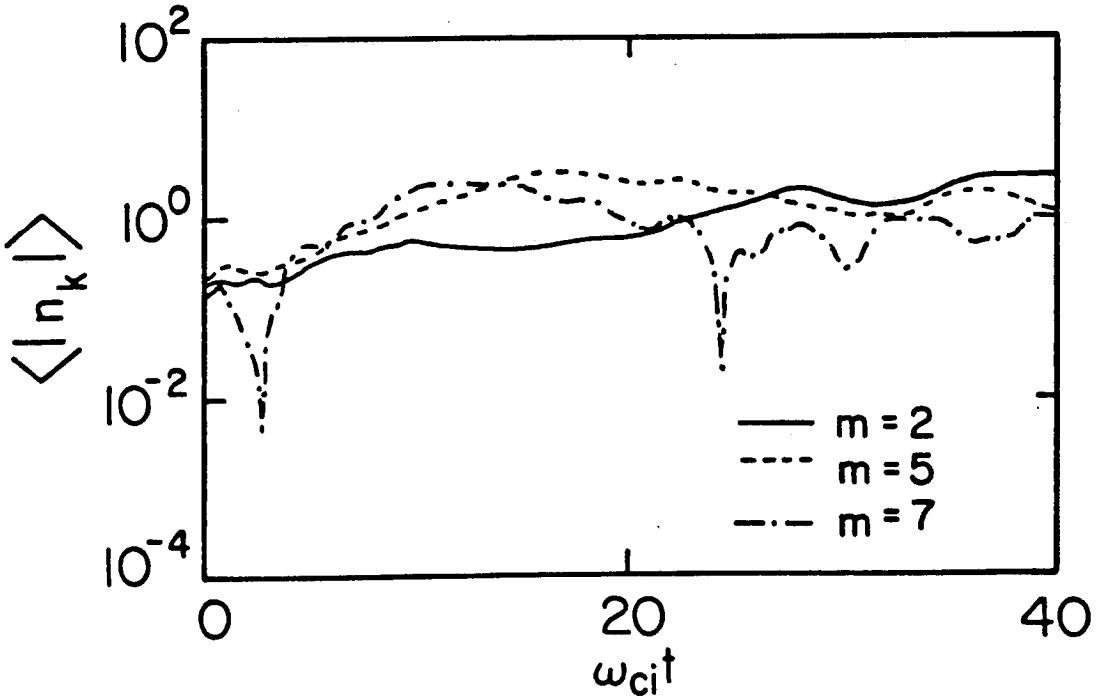
$\langle |n_k| \rangle$
10^2
10^0
10^{-2}
10^{-4}
0
20
40
$\omega_{ci} t$
m = 2
m = 5
m = 7

Fig. 3

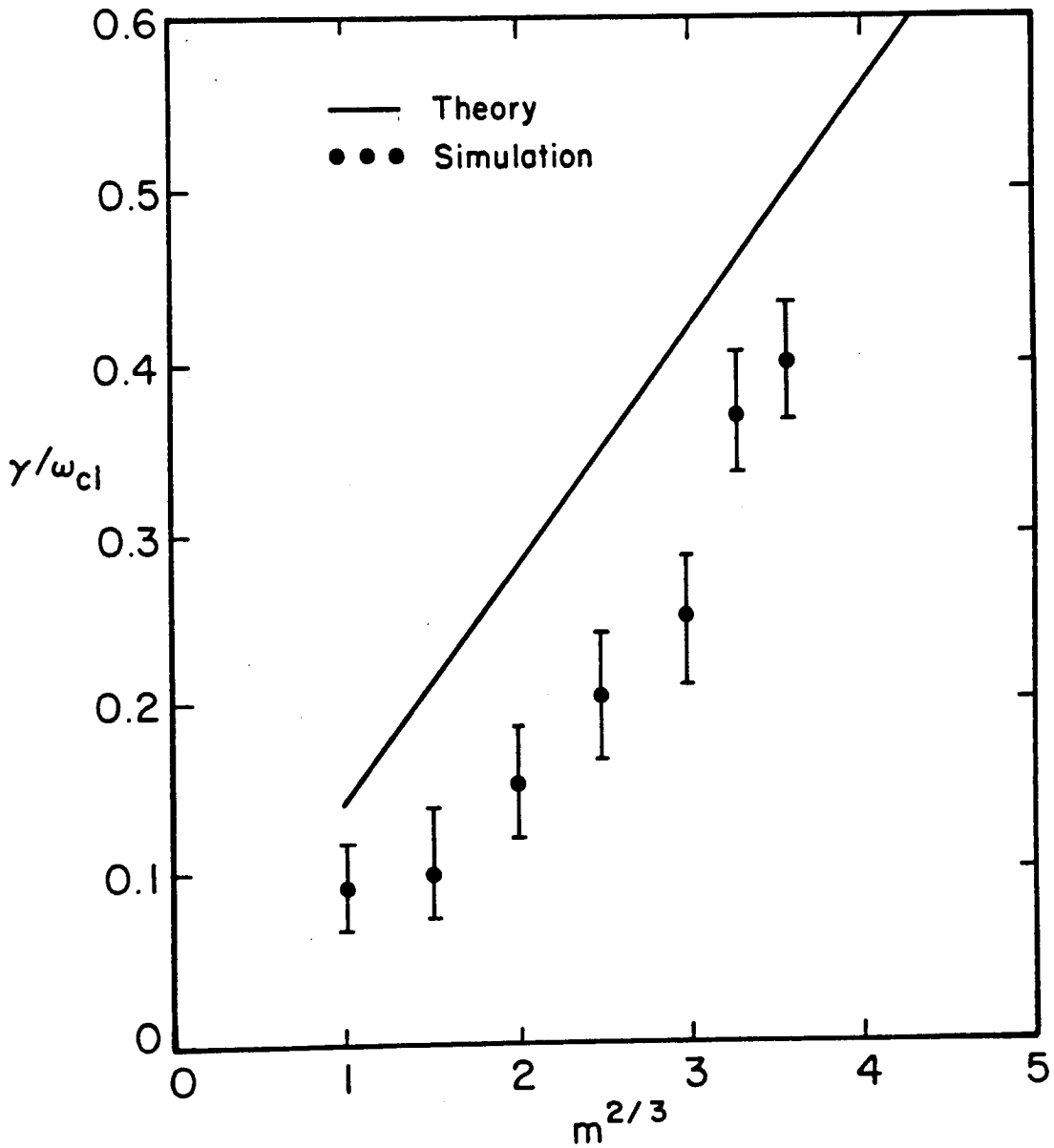
0.6
0.5
0.4
0.3
0.2
0.1
0
γ/ω_{cl}
Theory
Simulation
0
1
2
3
4
5
$m^{2/3}$

Fig. 4

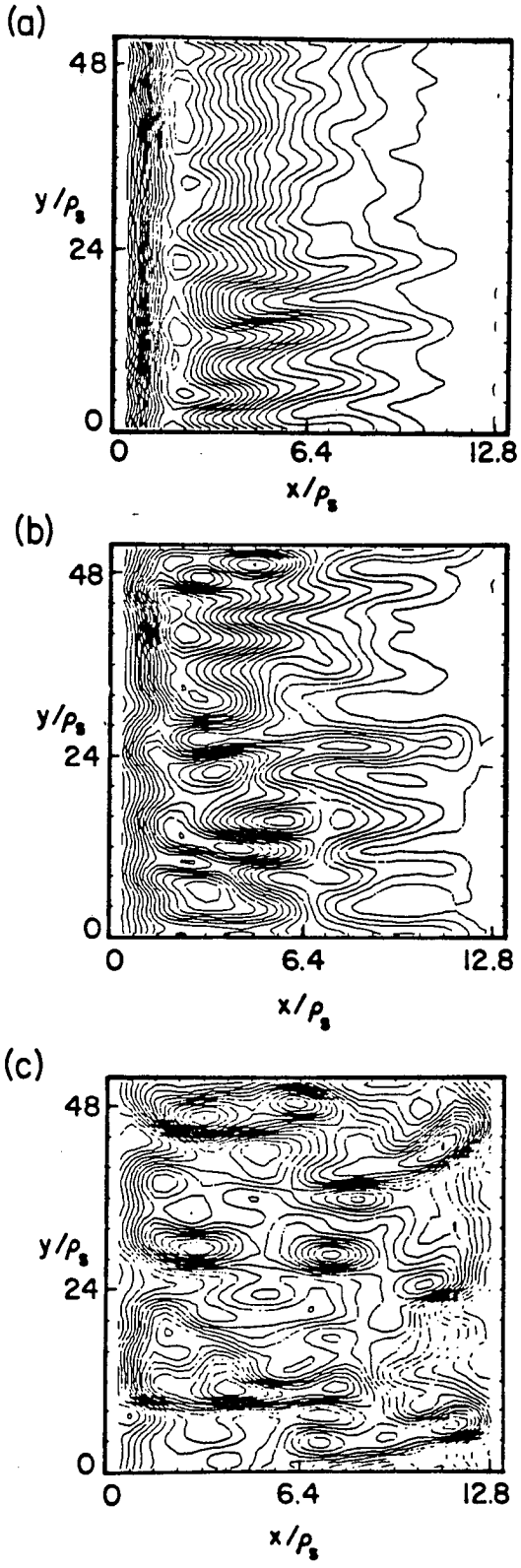
(a)
48
y/ρs
24
0
0
6.4
12.8
x/ρs
(b)
48
y/ρs
24
0
0
6.4
12.8
x/ρs
(c)
48
y/ρs
24
0
0
6.4
12.8
x/ρs

Fig. 5

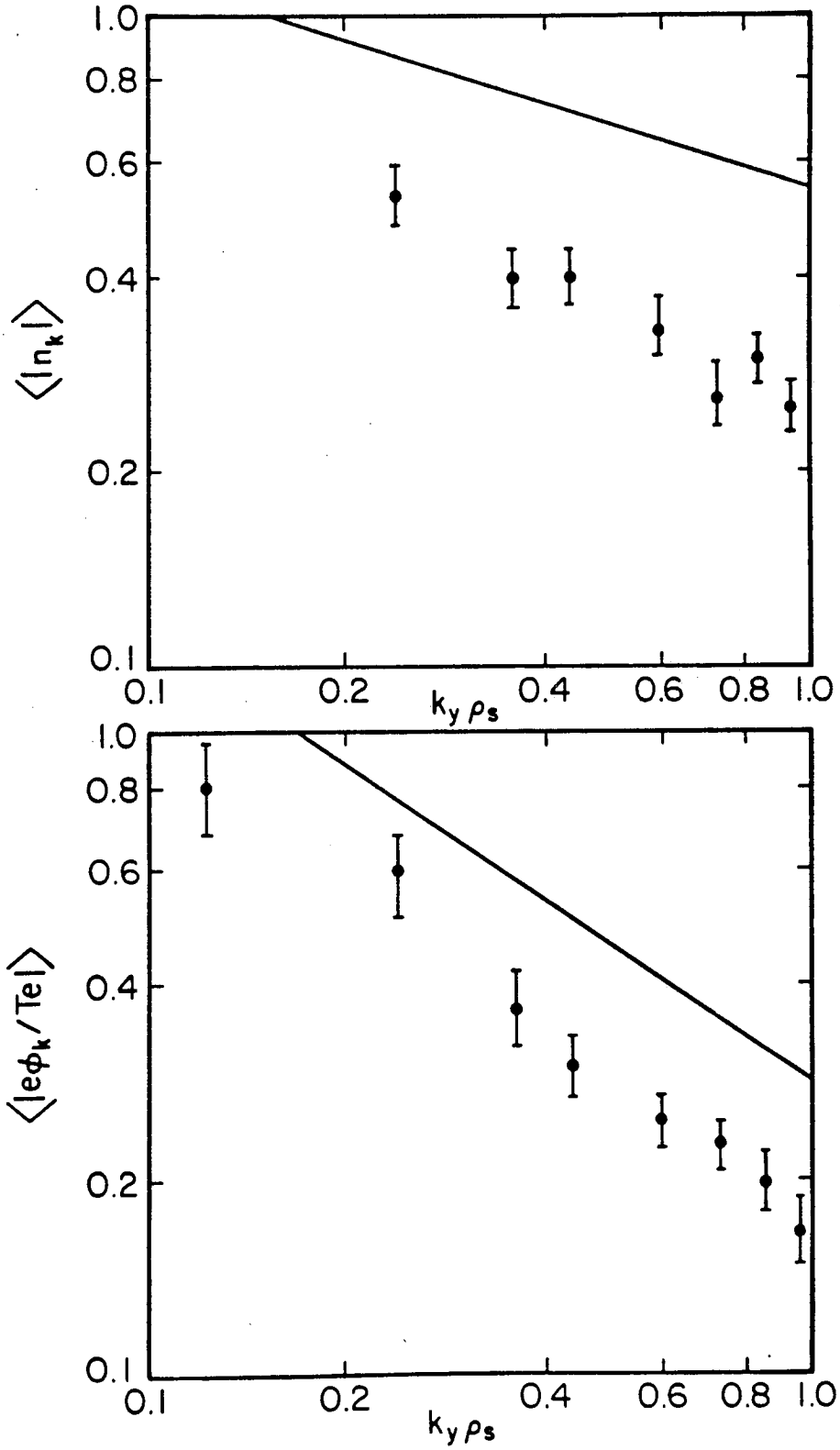
1.0
0.8
0.6
0.4
0.2
0.1
$\langle |n_k| \rangle$
0.1
0.2
$k_y \rho_s$
0.4
0.6
0.8
1.0
1.0
0.8
0.6
0.4
0.2
0.1
$\langle |e\phi_k / Te| \rangle$
0.1
0.2
$k_y \rho_s$
0.4
0.6
0.8
1.0

Fig. 6

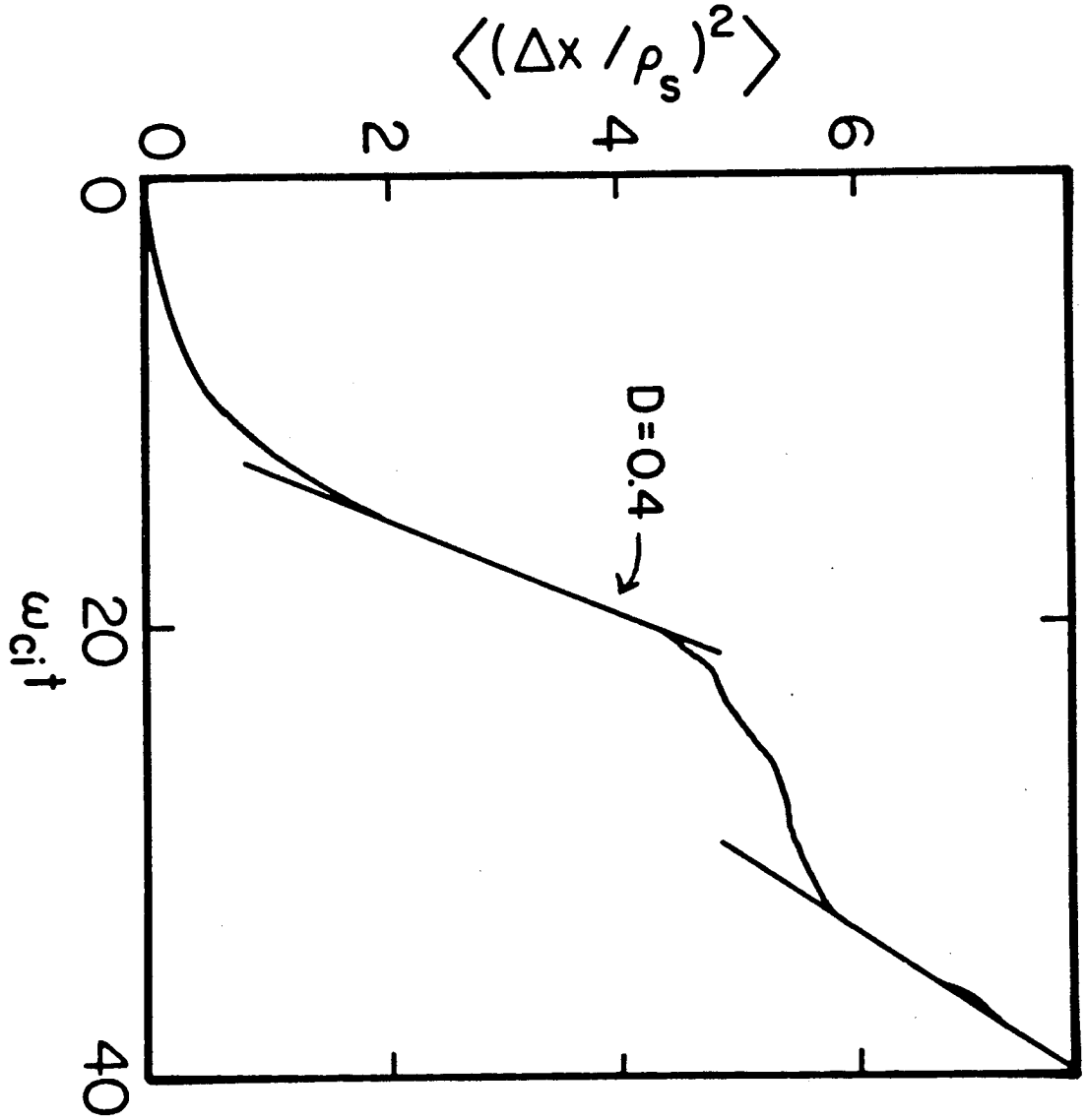

Fig. 7

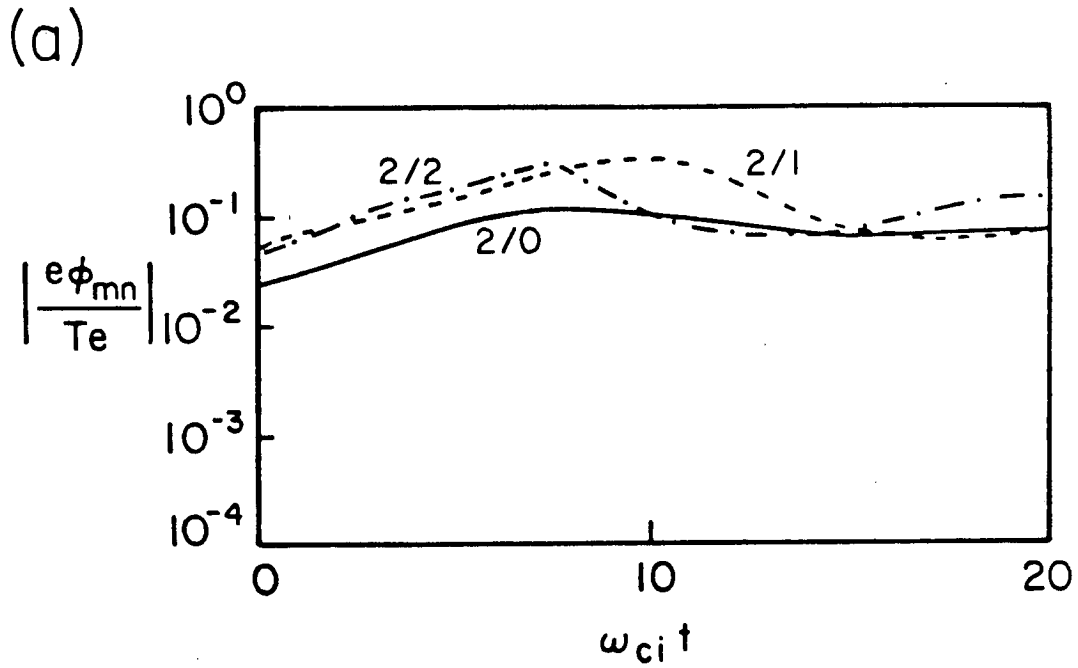
(a)
10^0
10^{-1}
10^{-2}
10^{-3}
10^{-4}
$\left|\frac{e\phi_{mn}}{Te}\right|$
2/2
2/1
2/0
0
10
20
$\omega_{ci}\,t$

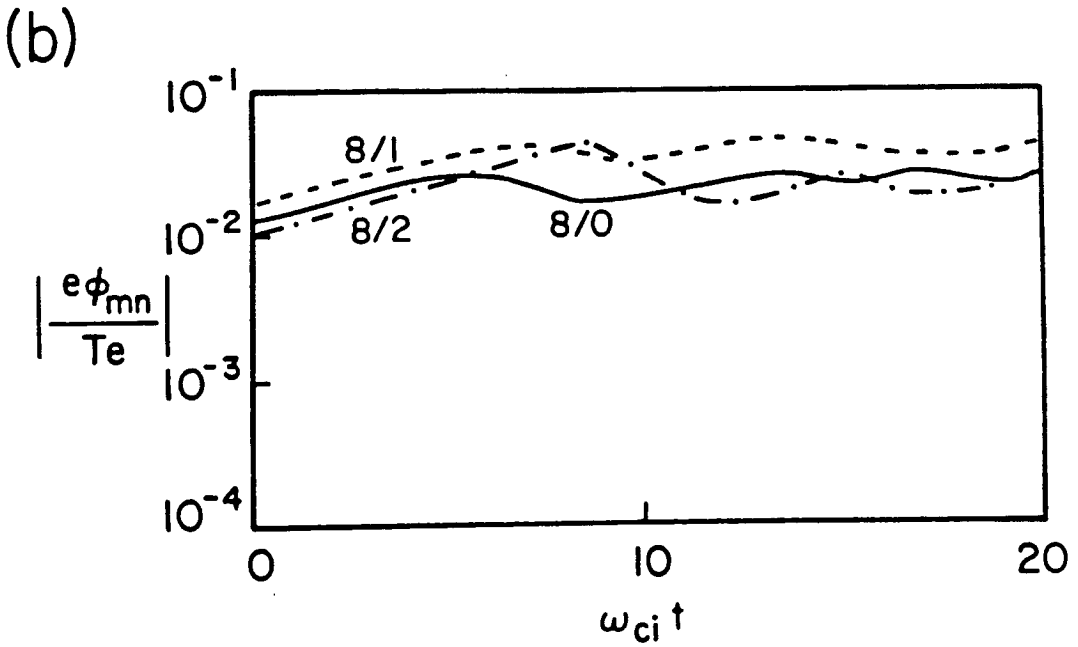
(b)
10^{-1}
10^{-2}
10^{-3}
10^{-4}
$\left|\frac{e\phi_{mn}}{Te}\right|$
8/1
8/2
8/0
0
10
20
$\omega_{ci}\,t$

Fig. 8

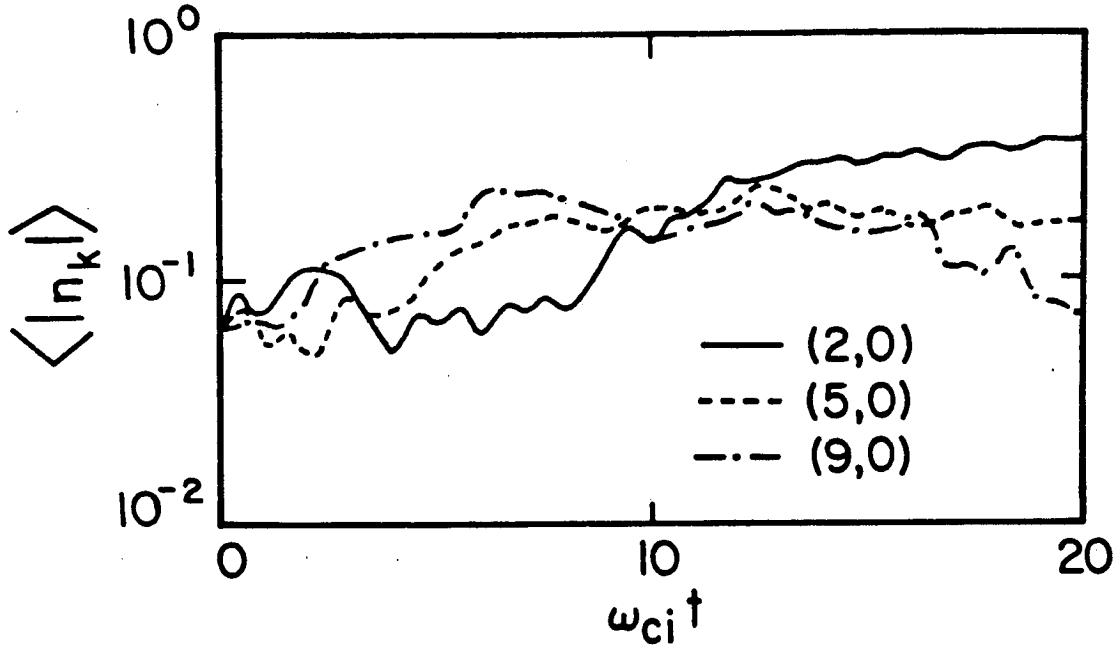
10^0
10^{-1}
10^{-2}
$\langle |n_k| \rangle$
(2,0)
(5,0)
(9,0)
0
10
20
$\omega_{ci} t$

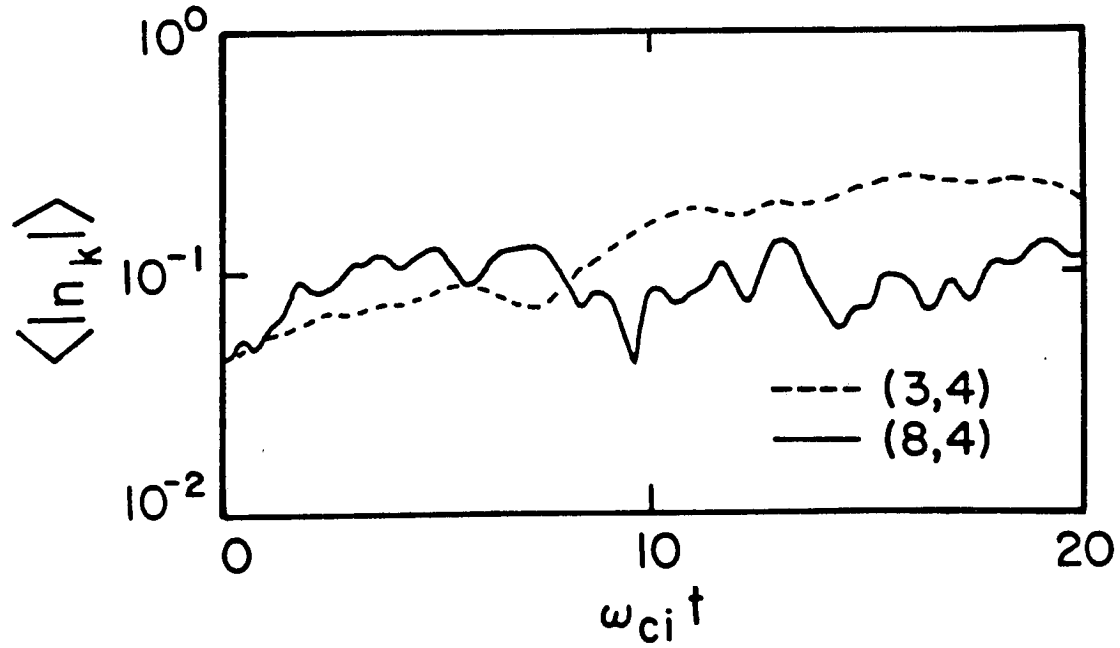
10^0
10^{-1}
10^{-2}
$\langle |n_k| \rangle$
(3,4)
(8,4)
0
10
20
$\omega_{ci} t$

Fig. 9

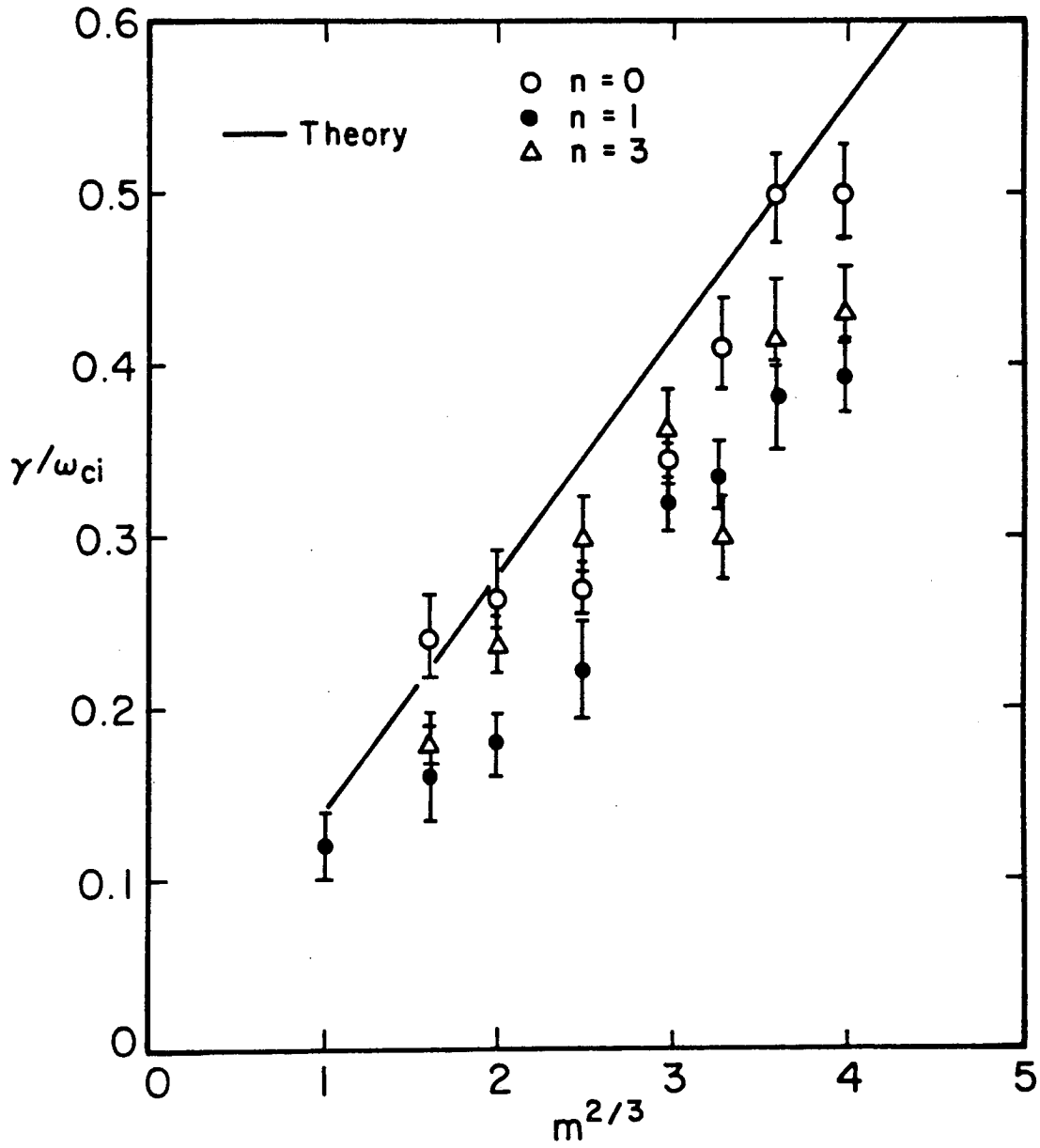

Fig. 10

(a)

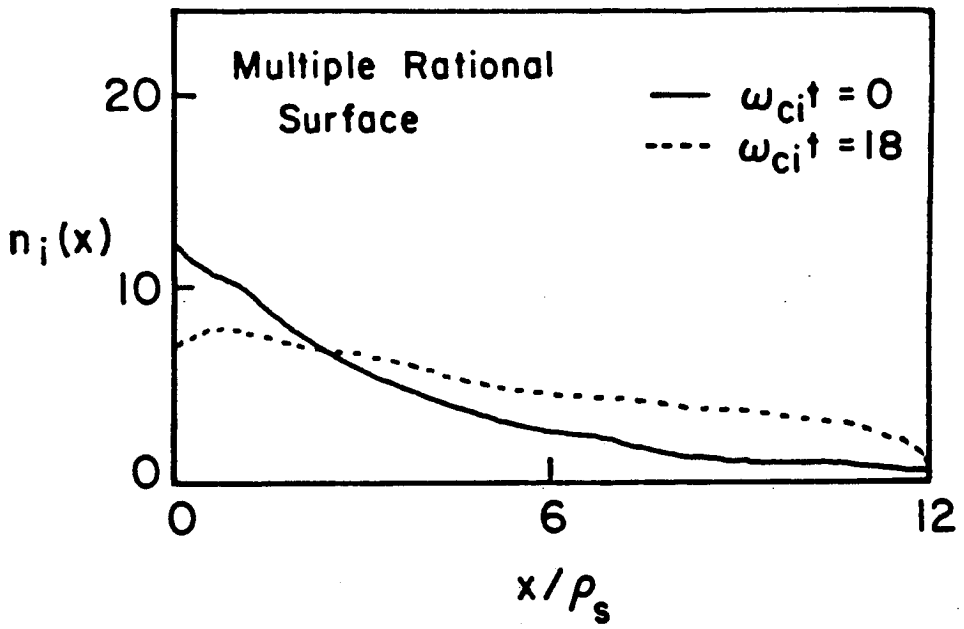
Multiple Rational Surface
$\omega_{ci}t = 0$
$\omega_{ci}t = 18$
$n_i(x)$
20
10
0
0
6
12
x/ρ_s

(b)

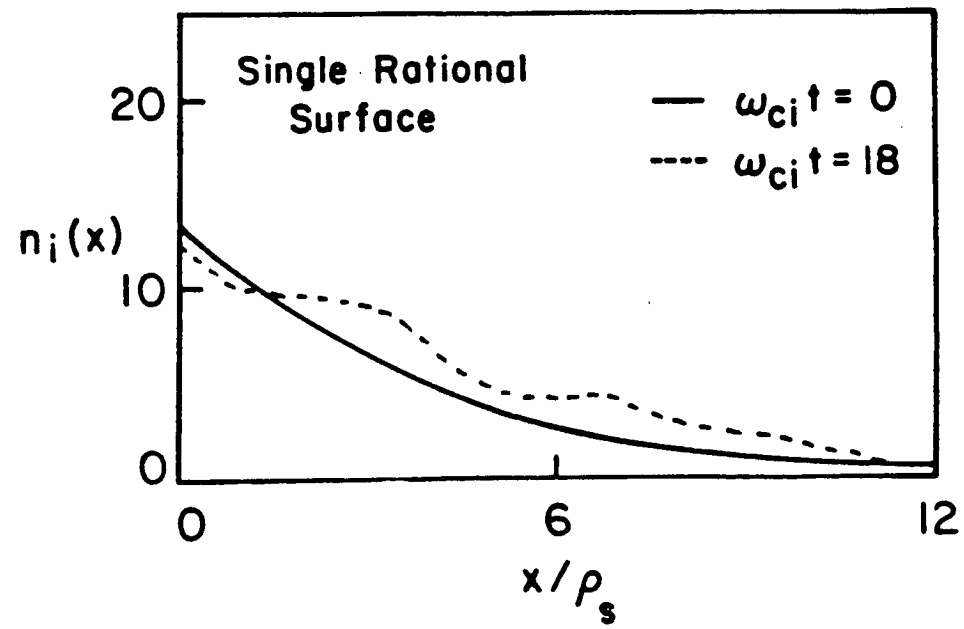
Single Rational Surface
$\omega_{ci}t = 0$
$\omega_{ci}t = 18$
$n_i(x)$
20
10
0
0
6
12
x/ρ_s

Fig. 11

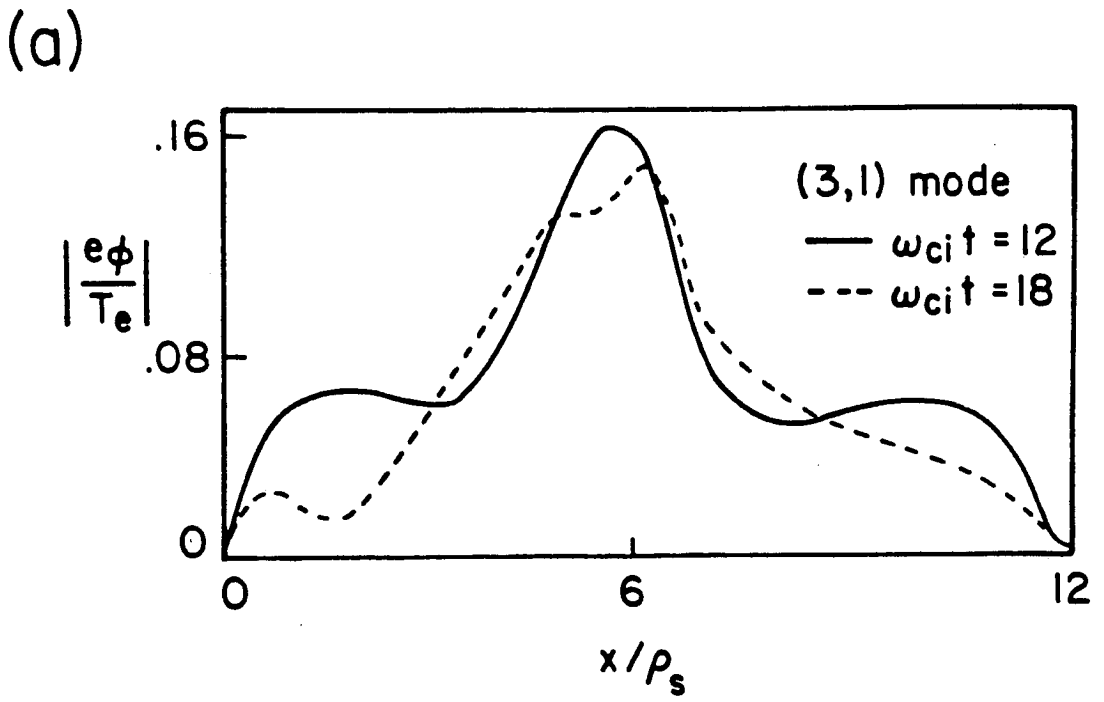
(a)
.16
.08
0
$\left|\frac{e\phi}{T_e}\right|$
(3,1) mode
$\omega_{ci}t = 12$
$\omega_{ci}t = 18$
0
6
12
x/ρ_s

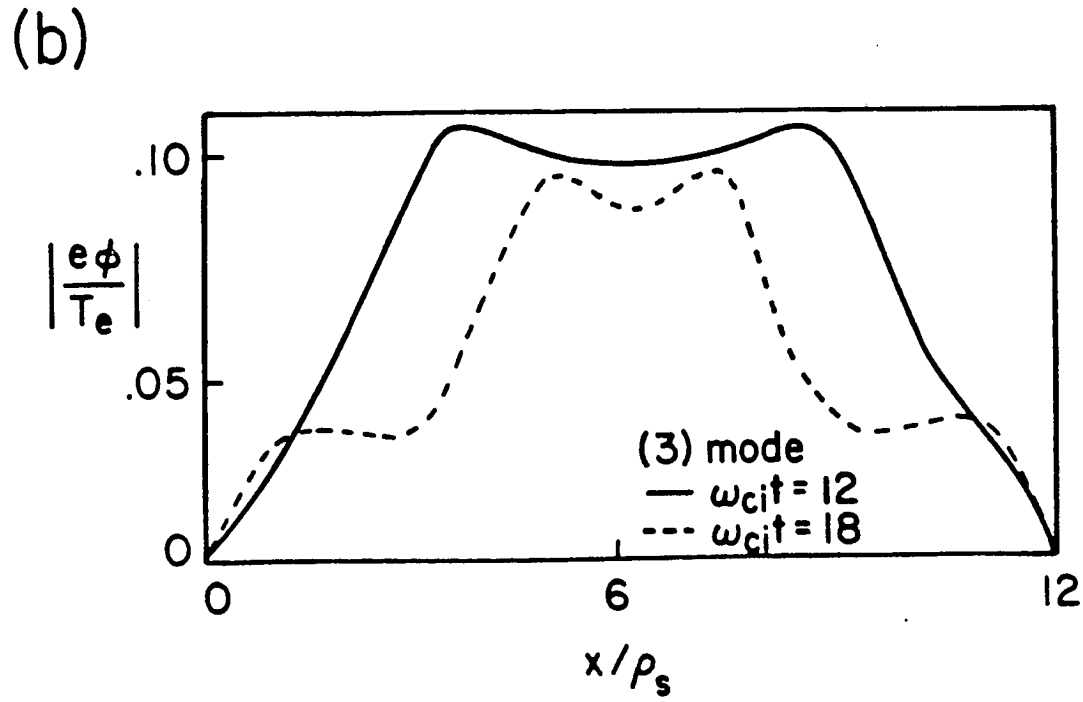
(b)
.10
.05
0
$\left|\frac{e\phi}{T_e}\right|$
(3) mode
$\omega_{ci}t = 12$
$\omega_{ci}t = 18$
0
6
12
x/ρ_s

Fig. 12

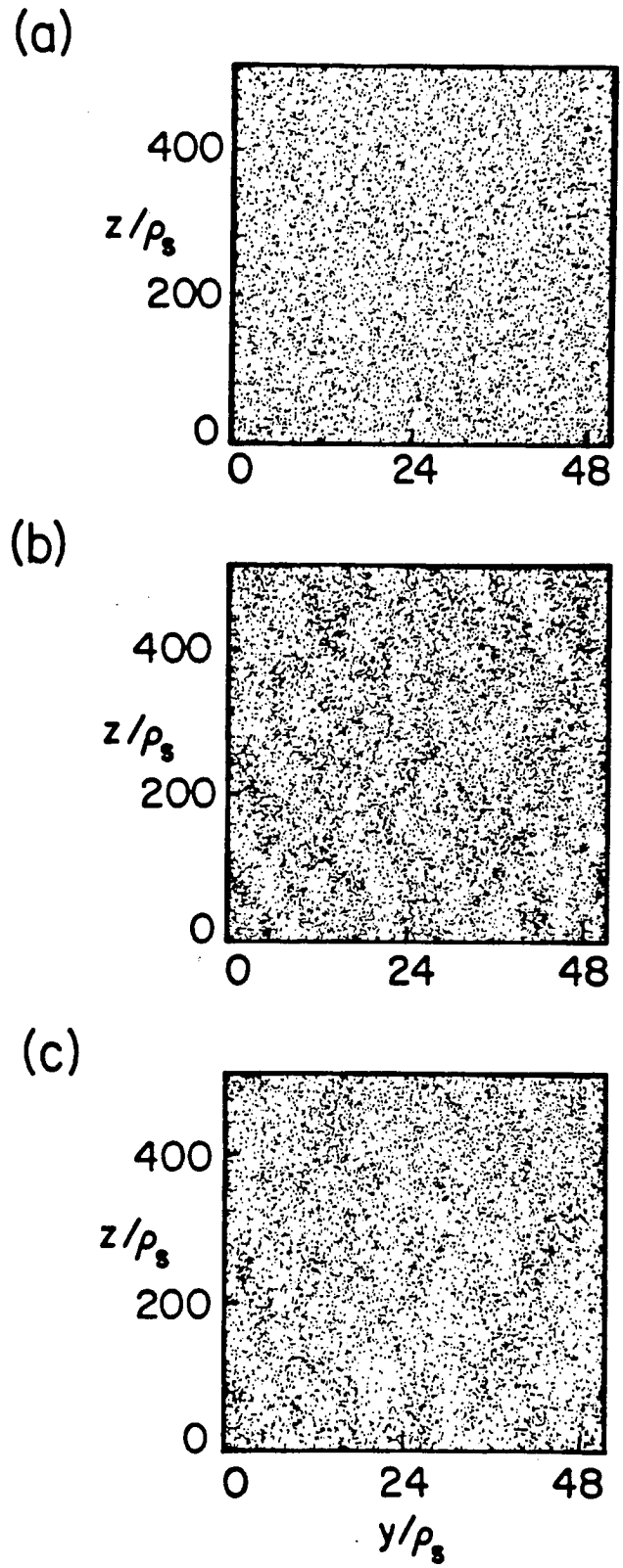
(a)
400
z/ρs
200
0
0
24
48
(b)
400
z/ρs
200
0
0
24
48
(c)
400
z/ρs
200
0
0
24
48
y/ρs

Fig. 13

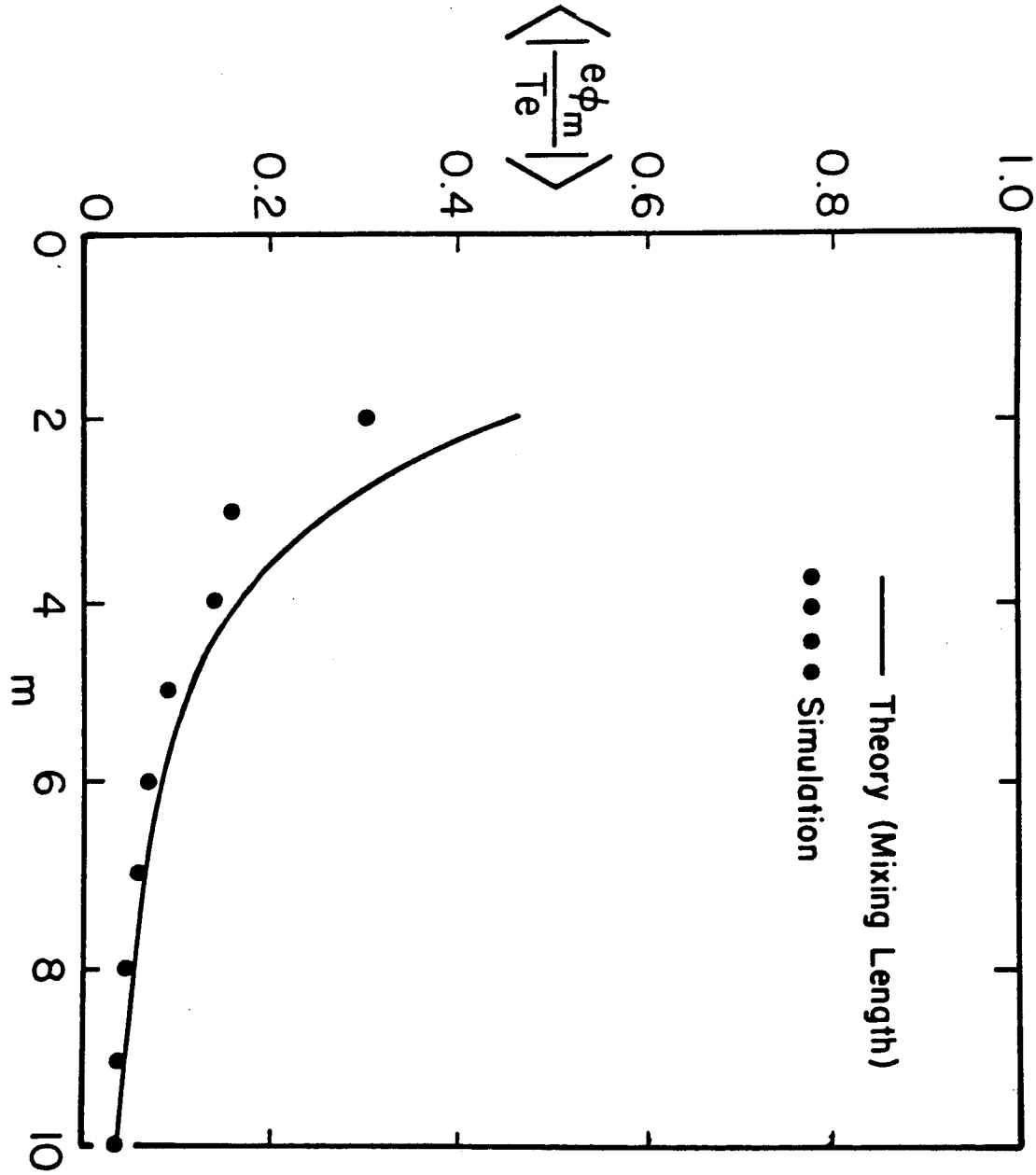
0
0.2
0.4
0.6
0.8
1.0
$\left\langle \left| \frac{e\phi_m}{Te} \right| \right\rangle$
0
2
4
6
8
10
m
Theory (Mixing Length)
Simulation

Fig. 14

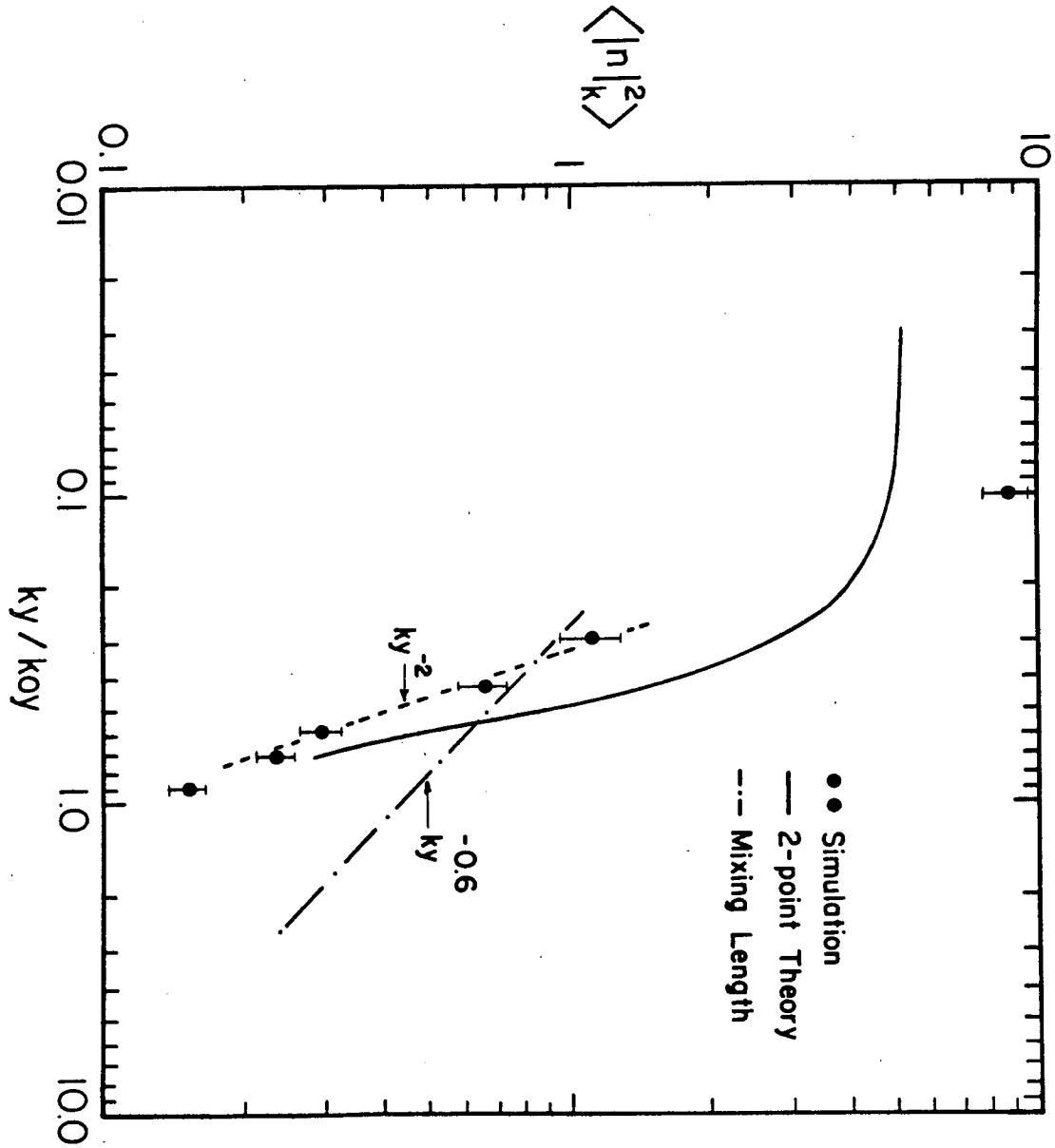
$\langle |n|^2_k \rangle$
ky / koy
0.1
0.01
0.1
1.0
10.0
1
10
ky -2
ky -0.6
Simulation
2-point Theory
Mixing Length

Fig. 15